# 7 Boundary Conditions and Surface Forcings

Without a bottom boundary on the atmosphere there would be no boundary layer. Friction at the surface slows the wind, and heat and moisture fluxes from the surface modify the state of the boundary layer. The heat and moisture fluxes are driven, in turn, by the external forcings such as radiation from the sun or transpiration from plants. Forcings across the top of the boundary layer also alter mean characteristics within it.

In this chapter we examine some of the external forcings, and show how those forcings and fluxes can be parameterized. Unfortunately, we cannot use any of the methods discussed in Chapter 6, because those methods apply only within a volume of air. For fluxes between a solid surface and air, we need to develop a different set of parameterizations, such as are discussed below.

## 7.1 Effective Surface Turbulent Flux

Turbulence by itself cannot transfer heat, momentum, or moisture across the interface from the ocean or from the earth. After all, it is rather infrequently that we see clods of soil jumping up and down in turbulent motion. Even ocean waves and turbulence have little direct coupling to atmospheric turbulence. Consequently, we must consider molecular effects, in addition to turbulent transport.

Molecular conduction of heat, molecular diffusion of tracers, and molecular viscous transfer of momentum cause transport between the surface and the lowest millimeters of air. Once in the air, turbulence takes over to transport momentum, heat and other constituents to greater depths in the atmosphere. The molecular and turbulent transport processes work together as sketched in Fig 7.1.

To simplify our equations for boundary layer evolution, we find it convenient to define an ***effective turbulent flux*** that is the sum of the molecular and turbulent fluxes. At the surface where there is no turbulent flux, the ***effective surface***

***turbulent flux*** has a magnitude equal to that of the molecular flux. Above the lowest few centimeters, however, the molecular contribution is so small that it can be neglected compared to the turbulent flux.

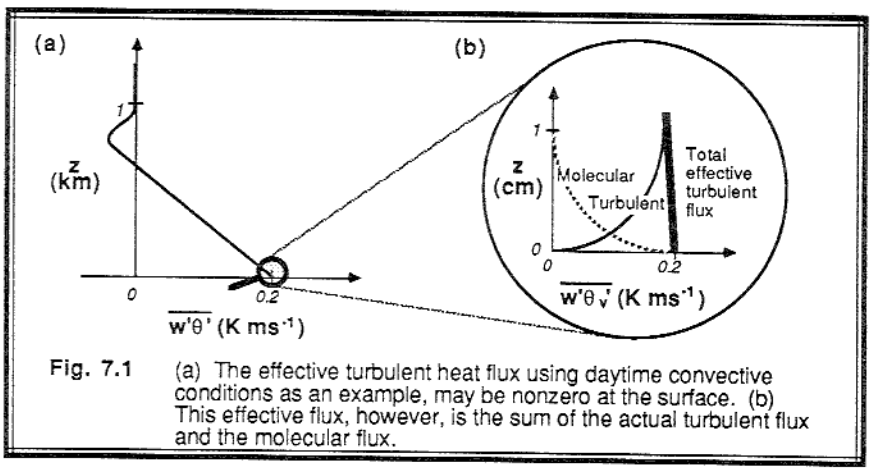


**Fig. 7.1** (a) The effective turbulent heat flux using daytime convective conditions as an example, may be nonzero at the surface. (b) This effective flux, however, is the sum of the actual turbulent flux and the molecular flux.

The thin layer of air in which molecular processes dominate is called the ***micro layer***. Within this layer, molecular transport, such as conduction of heat, can be described by:

$$Q_H = - \nu_\theta \frac{\partial T}{\partial z} \tag{7.1}$$

where $\nu_\theta$ is the molecular thermal diffusivity (on the order of $2 \times 10^{-5}$ m$^2$s$^{-1}$ for air). For a typical kinematic heat flux of 0.2 K·m·s$^{-1}$, (7.1) tells us that a temperature gradient of $1 \times 10^4$ K·m$^{-1}$ is required. This corresponds to a 10 °C temperature difference across a micro layer 1 mm thick.

Such large gradients are indeed observed. Those of you who have walked barefoot across a black asphalt road on a sunny summer day can testify that the surface "skin" temperature can become burning hot to the touch, even though the air temperature may be a pleasant 25 or 30 °C. The hot skin temperature can create a large temperature gradient in the lowest millimeters of air. These large gradients in the micro layer are also the cause of the mirage that we sometimes see over highways.

From this point on, whenever we refer to a surface turbulent flux in this text, we are really implying a surface ***effective*** flux. In this way, we can ignore the molecular processes, and just use turbulence equations such as (3.5.3) with the effective flux. As shown in Chapters 1, 3 and 4, the effective flux varies by only a small portion of its magnitude in the lowest tens of meters of the BL. Thus, the turbulent flux measured at the standard "surface" instrument shelter (screen) height of 2 m provides a good approximation to the effective surface turbulent flux.

## 7.2 Heat Budget at the Surface

Picture a layer of air with its top just above the highest trees (or ocean wave crests) in a region, and its base just below the earth's surface (or below the wave troughs), as sketched in Fig 7.2a. This layer has turbulent energy transfer with the air above it, radiative transfer through the top of it, and molecular energy transfer into the soil (or sea) below.

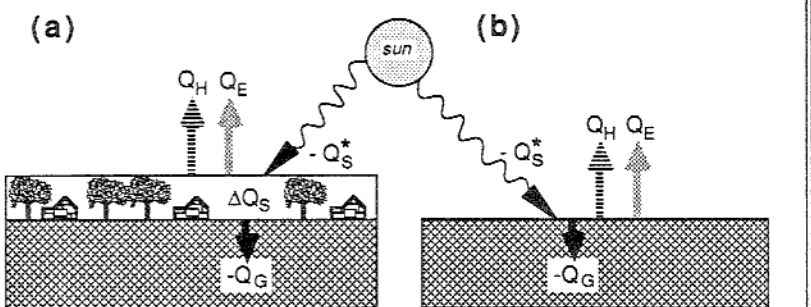


**Fig. 7.2** Contributions to the surface energy balance (a) for a finite thickness box and (b) for an infinitesimally thin layer. $-\bar{Q}^*_S$ is the net radiative contribution, $Q_H$ is turbulent sensible heat flux, $Q_E$ is turbulent latent heat flux, $-Q_G$ is molecular flux into the ground, and $\Delta Q_S$ is storage.

The energy budget for this layer, where upward fluxes are positive, is:

$$-\bar{Q}^*_s = \bar{Q}_H + \bar{Q}_E - \bar{Q}_G + \Delta\bar{Q}_S \qquad (7.2a)$$

or

$$-Q^*_s = Q_H + Q_E - Q_G + \Delta Q_S \qquad (7.2b)$$

where
- $Q^*_s$ = net upward radiation at the surface
- $Q_H$ = represents the upward sensible heat flux out of the top
- $Q_E$ = represents the upward latent heat flux out of the top
- $Q_G$ = represents the upward molecular heat flux into the bottom
- $\Delta Q_S$ = denotes the storage or intake of internal energy (positive for warming and for chemical storage by photosynthesis).

In simple terms, this is nothing more than energy ***in*** balancing energy ***out*** and ***storage***. The external forcing is $Q^*_s$, and all the other terms are response terms.

Equation (7.2a) is in energy flux units such as $J \cdot m^{-2} s^{-1}$ or $W \cdot m^{-2}$, while (7.2b) is in kinematic units such as $K \cdot m \cdot s^{-1}$. Thus, the second equation is just the first equation divided by $\rho C_p$. From section 2.6, we recall that $Q_H = (\overline{w'\theta'})_s$, and $Q_E = (L_v/C_p) \cdot (\overline{w'q'})_s$.

Very complex processes can occur within our imaginary layer (Geiger, 1965; Oke, 1978; Brutsaert, 1985), such as: radiation between leaves, plants, buildings, and animals; turbulent circulations different from those higher in the boundary layer; vertical variations of the sensible and latent heat flux associated with evaporation and condensation; and transpiration. Because of this complexity, we have employed the simplification of a layer into which the net effect of all of these processes can be lumped together as $\Delta Q_S$.

Sometimes, we prefer to conceptually employ an infinitesimally thin layer, as sketched in Fig 7.2b. This is not a really layer, but a plane. The resulting ***surface heat budget*** is

$$-Q_s^* = Q_H + Q_E - Q_G \tag{7.2c}$$

There can be no storage because there is no mass contained within a zero thickness layer.

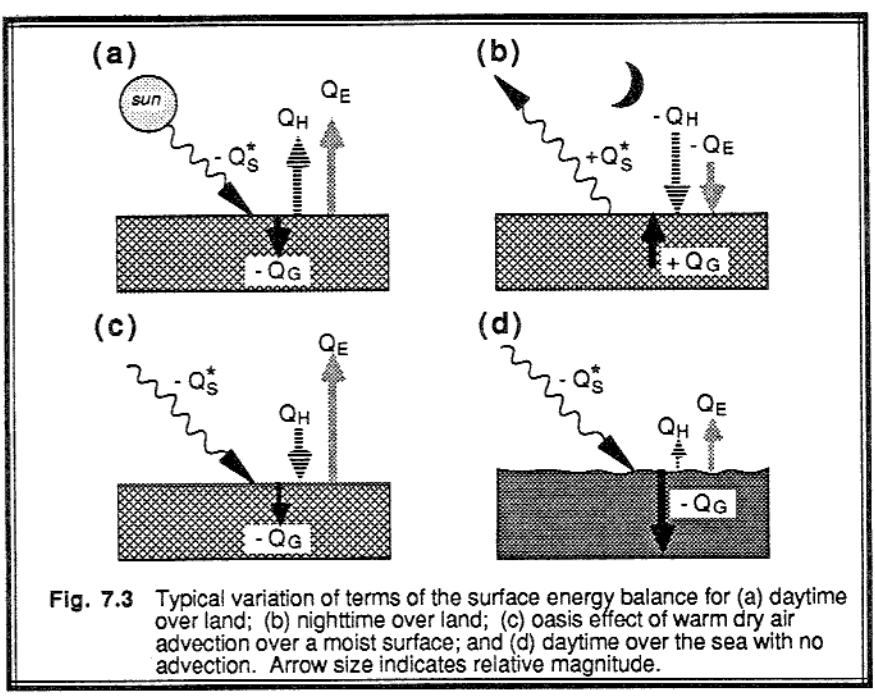


**Fig. 7.3** Typical variation of terms of the surface energy balance for (a) daytime over land; (b) nighttime over land; (c) oasis effect of warm dry air advection over a moist surface; and (d) daytime over the sea with no advection. Arrow size indicates relative magnitude.

The neglect of the storage layer works well for quasi-steady-state situations where there is no appreciable change in the mean temperature of that layer. It also works well for flat barren land surfaces, and for waveless sea surfaces.

During a late morning sunny ***day over land***, $-Q^*_s$ is positive because there is more downward radiation entering the layer than leaving upward. $Q_H$ and $Q_E$ are positive because of heat and moisture transport away upward from the surface. $-Q_G$ is positive when heat is conducted downward into the ground from the warm surface (see Fig 7.3a).

At ***night over land***, $-Q^*_s$ is often negative because of the net upward longwave radiative cooling to space. $Q_H$ is negative because of a downward heat flux from the air. Dew or frost formation makes $Q_E$ negative. Conduction of heat from the warm ground up to the cooler surface makes $-Q_G$ negative. The release of stored heat from the layer makes $\Delta Q_S$ negative (see Fig 7.3b).

The daytime and nighttime examples above demonstrate a classical behavior where the budget terms were either all positive during the day, or all negative at night. Typical diurnal evolution of terms in (7.2a) is shown in Fig 7.4 for a vegetated land surface at mid latitudes.

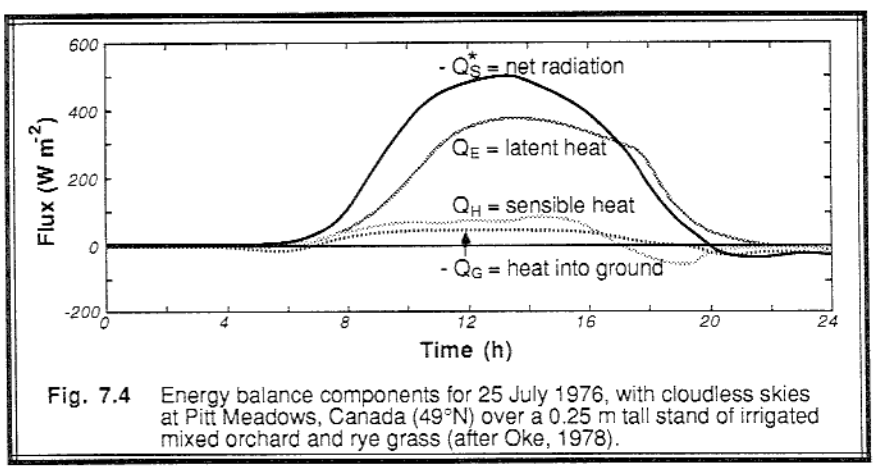


**Fig. 7.4** Energy balance components for 25 July 1976, with cloudless skies at Pitt Meadows, Canada (49°N) over a 0.25 m tall stand of irrigated mixed orchard and rye grass (after Oke, 1978).

Other nonclassical situations occur in nature, such as the ***oasis effect***. Picture warm dry air blowing over a cool moist oasis (Fig 7.3c). There is strong evaporation from the moist ground and plants into the air, resulting in latent cooling that keeps the oasis at a pleasant temperature. However, this upward latent heat flux is opposed by a downward sensible heat flux from the warm air to the cool ground. Thus, $Q_E$ and $-Q^*_s$ are positive, while $Q_H$ is negative. If we focus on just these three terms, we see that the latent heat flux can be greater in magnitude than the solar heating, because of the additional energy that is extracted from the warm air by evaporation.

The ocean budget behaves differently than the land budget because turbulence in the water can efficiently transport heat away from the surface and distribute it deeper in the

water. Also, the heat capacity ($\rho C_v$) of water is about 4000 times larger than that of air, meaning that a lot of heat can be absorbed into water with little temperature change. Thus, the diurnal cycle of radiation is almost completely balanced by a corresponding diurnal variation of energy transport into the sea (Fig 7.3d). In addition, the nearly constant sea surface temperature with time results in a nearly constant heat and moisture flux, and associated slow temporal changes in air temperature and humidity.

## 7.3 Radiation Budget

It is often convenient to split the net radiation term into four components:

$$Q^* = K\uparrow + K\downarrow + I\uparrow + I\downarrow \tag{7.3}$$

where $K\uparrow$ = upwelling ***reflected*** short wave (solar) radiation
$K\downarrow$ = downwelling shortwave radiation ***transmitted*** through the air
$I\uparrow$ = longwave (infrared, IR) radiation ***emitted*** up
$I\downarrow$ = longwave ***diffusive*** IR radiation down

The downward fluxes are negative by definition, and upward are positive. Each of these terms represents the sum of direct and diffuse radiation components crossing a locally horizontal plane such as the surface. Fig 7.5 shows a typical diurnal cycle for these radiation components in clear skies at a land surface. Although this equation was written here in kinematic flux form where each term has units of $K \cdot m \cdot s^{-1}$, it could also have been written in energy flux form.

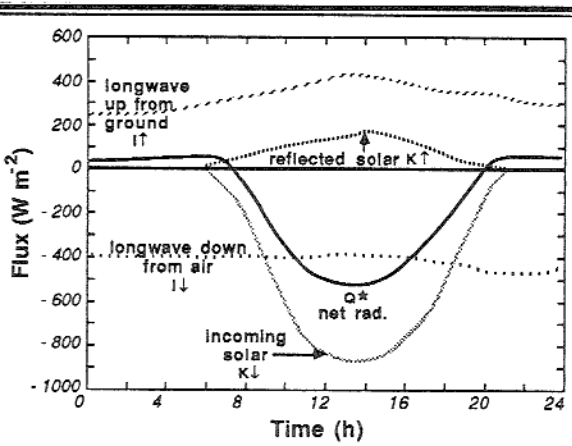


**Fig. 7.5** Surface radiation budget components for 30 July 1971, at Matador, Saskatchewan (50°N) over a 0.2 m stand of native grass. Cloudless skies in the morning, increasing clouds in the late afternoon and evening (after Ripley and Redmann, 1976).

Splitting radiation into only two wavelength bands (short and longwave) is possible because the peak in the solar spectrum is at the normal visible light wavelengths, while the earth/atmosphere system is emitting infrared radiation characteristic of its absolute

temperature (in the range of 280 K at the surface to about 245 K at the top of the atmosphere). Since there are no other bodies near the earth that contribute significantly to the radiation budget, we need only be concerned with those two bands.

### 7.3.1 Shortwave Radiation

The intensity of incoming solar radiation at the top of the atmosphere is called the ***solar irradiance***, S. Although it was formerly known as the ***solar constant,*** this term is being used less frequently because of the realization that the solar irradiance is not constant — ranging from about -1360 to -1380 $W \cdot m^{-2}$. We will use a value of $S = -1370$ $W \cdot m^{-2}$ (Kyle, et al., 1985), or $S = -1.127$ $K \cdot m \cdot s^{-1}$ in kinematic units, where the density and specific heat of air in the boundary layer is used for the conversion to kinematic units.

Some of this radiation is attenuated by scattering, absorption, and reflection from clouds on the way down to the surface. When the sun is lower in the sky, the radiation will also be attenuated by its longer path through the atmosphere en route to the surface. Define $T_K$ as the net sky ***transmissivity***, or the fraction of solar radiation that makes it to the surface. Define $\Psi$ as the solar elevation angle; namely, the angle of the sun above the local horizon. One simple parameterization (Burridge and Gadd, 1974) for the transmissivity is:

$$T_K = (0.6 + 0.2 \sin \Psi) \cdot (1 - 0.4\, \sigma_{C_H}) \cdot (1 - 0.7\, \sigma_{C_M}) \cdot (1 - 0.4\, \sigma_{C_L}) \qquad (7.3.1a)$$

where $\sigma_C$ represents the cloud-cover fraction, and where subscripts H, M, and L signify high, middle, and low clouds respectively. When the sun is directly overhead and there are no clouds, $T_K = 0.80$ . If the sun is overhead but there are overcast clouds at all three levels, then $T_K = 0.086$.

The solar elevation angle is also important because when it is less than 90°, the radiation that does reach the surface is spread out over a larger area, reducing the radiation per unit surface area by a factor of $\sin \Psi$. The expression for downwelling radiation at the surface is approximately

$$\begin{aligned} K{\downarrow}_s &= S \cdot T_K \cdot \sin \Psi && \text{for daytime (i.e., } \sin \Psi \text{ positive)} \\ &= 0 && \text{for nighttime (i.e., } \sin \Psi \text{ negative)} \end{aligned} \qquad (7.3.1b)$$

Determination of the local elevation angle is a straightforward exercise in geometry (Zhang and Anthes, 1982), resulting in:

$$\sin \Psi = \sin \phi \sin \delta_s - \cos \phi \cos \delta_s \cos\left[\left(\frac{\pi\, t_{UTC}}{12}\right) - \lambda_e\right] \qquad (7.3.1c)$$

where $\phi$ and $\lambda_e$ are the latitude (positive north) and longitude (positive west) in radians,

$\delta_s$ is the ***solar declination angle*** (angle of the sun above the equator, in radians), and $t_{UTC}$ is Coordinated Universal Time in hours. The solar declination angle is

$$\delta_s = \phi_r \cos\left[\frac{2\pi\,(d - d_r)}{d_y}\right] \qquad (7.3.1d)$$

where $\phi_r$ is the latitude of the Tropic of Cancer (23.45° = 0.409 radians), d is the number of the day of the year (e.g., October 27 = day 300), $d_r$ is the day of the summer solstice (173), and $d_y$ is the average number of days per year (365.25).

Define the ***albedo***, a, as the fraction of downwelling radiation at the surface that is reflected. The albedo varies from about 0.95 over fresh snow, 0.4 over light-colored dry soils, 0.2 over grass and many agriculture crops, 0.1 over coniferous forests, to 0.05 over dark wet soils. The upwelling (reflected) radiation is thus

$$K\uparrow_s = -\,a\,K\downarrow_s \qquad (7.3.1e)$$

The albedo of water not only varies with wave state, but is a strong function of sun angle (Krauss, 1972). When the sun is directly overhead over a smooth water surface, the albedo is about 0.05, while it increases to nearly 1.0 at low elevation angles.

### 7.3.2 Longwave Radiation

As is obvious in Fig 7.5, the upward and downward longwave radiation terms are both large, but of opposite sign. Also, they do not vary much with time in clear sky conditions. As a result, the ***net longwave radiation*** ($I^* = I\uparrow + I\downarrow$) is approximately constant with time, and is often negative because of the net radiative loss from the earth/atmosphere system to space.

When clouds are present, much of the outgoing radiation can be balanced by downward radiation from the clouds. Low clouds are more effective at this than high clouds. For overcast clouds at all three levels, we might expect the net radiation to be approximately zero.

The net upward longwave radiation at the surface is sometimes approximated (Burridge and Gadd, 1974) by :

$$I^* = (0.08\ \mathrm{Kms^{-1}})\ (1 - 0.1\sigma_{C_H} - 0.3\,\sigma_{C_M} - 0.6\,\sigma_{C_L}) \qquad (7.3.2a)$$

This type of parameterization is known to be an oversimplification of the actual physics. Nevertheless, it is useful when detailed radiation parameterizations are not appropriate.

An alternative to parameterizing the net longwave radiation is to parameterize the $I\uparrow$ and $I\downarrow$ terms separately. The ***Stefan-Boltzmann law*** gives:

$$I\uparrow_s = \varepsilon_{IR}\,\sigma_{SB}\,T^4 \qquad (7.3.2b)$$

where $\sigma_{SB} = 5.67\text{x}10^{-8}$ W·m$^{-2}$·K$^{-4}$ is the ***Stefan-Boltzmann constant.*** The infrared ***emissivity***, $\varepsilon_{IR}$, is in the range 0.9 to 0.99 for most surfaces.

The downward longwave radiation $I\downarrow$ is much more difficult to calculate, because one must vertically integrate the radiative flux divergence equations. Simple radiation models are discussed in Chapters 12 and 13.

Putting together the various parameterizations for short and longwave radiation yields the following approximation for net radiative flux at the surface:

$$\begin{aligned} Q^* &= (1 - a)\,S\,T_K \sin\Psi + I^* && \text{during daytime} \\ &= + I^* && \text{during nighttime.} \end{aligned} \qquad (7.3.2c)$$

where S is negative. One must remember that this is just one possible parameterization. Other equally good approximations have appeared in the literature.

### 7.3.3 Radiation Budget Example

**Problem**: Calculate the radiation budget terms for every hour during a 24-hour cycle, given the following scenario:

| | |
|---|---|
| location: | Madison, Wisconsin (latitude = 43.08°N, longitude = 89.42°W) |
| clouds: | none |
| date: | 5 November (day 309) |
| start time: | midnight local time. |
| average albedo: | 0.2 |

**Solution**: The following example was prepared, solved, and plotted using spreadsheet software, which is available for most microcomputer systems. Table 7-1 lists the spreadsheet results for this case.

First, the latitude and longitude was converted to radians, and the solar declination angle was found using (7.3.1d). This angle was -0.284 radians (-16.27°). The negative sign tells us that the northern hemisphere is in, or approaching, winter.

For each of the 24 hours, the local time was converted to UTC time. For this example, the conversion was done using longitudes rather than political time zones, knowing that it takes the earth 24 hours to rotate a full 360 degrees of longitude. Next, (7.3.1c) was used to find sin $\Psi$ (sinphi) at each time, where sinphi was set to zero whenever the sun was below the horizon. Next, the transmissivity $T_K$ was calculated using (7.3.1a). Then $K_{down}$ was found using (7.3.1b), and $K_{up}$ was found using (7.3.1e). The net longwave radiation, $I^*$, was found using (7.3.2a). Finally, the net radiation was calculated using $Q^* = K_{up} + K_{down} + I^*$, which is a form of (7.3).

**Table 7-1.** Example radiation calculation for Madison, Wisconsin.

Radiation Parameterization for: Madison, Wisconsin

Cloudcover:
Low = 0
Mid = 0
High = 0

| Location | (deg) | (rad) |
|---|---|---|
| Lat.= | 43.08 | 0.75189 |
| Long.= | 89.42 | 1.56067 |

| | | |
|---|---|---|
| Solar constant = | -1.127 | (Km/s) |
| Longwave max = | 0.08 | (Km/s) |
| Solar declination = | -0.2843 | (radians) |
| Albedo = | 0.2 | |

Time Date Info:
Date: 5 Nov
Day #: 309
Local start h 0
Timestep h 1

| Local (hr) | UTC (hr) | sinphi | Trans. | K down (Km/s) | Kup (Km/s) | I* (Km/s) | Q* (Km/s) |
|---|---|---|---|---|---|---|---|
| 0 | 5.96 | 0 | 0.6 | 0 | 0 | 0.08 | 0.080 |
| 1 | 6.96 | 0 | 0.6 | 0 | 0 | 0.08 | 0.080 |
| 2 | 7.96 | 0 | 0.6 | 0 | 0 | 0.08 | 0.080 |
| 3 | 8.96 | 0 | 0.6 | 0 | 0 | 0.08 | 0.080 |
| 4 | 9.96 | 0 | 0.6 | 0 | 0 | 0.08 | 0.080 |
| 5 | 10.96 | 0 | 0.6 | 0 | 0 | 0.08 | 0.080 |
| 6 | 11.96 | 0 | 0.6 | 0 | 0 | 0.08 | 0.080 |
| 7 | 12.96 | 0 | 0.6 | 0 | 0 | 0.08 | 0.080 |
| 8 | 13.96 | 0.1589 | 0.6318 | -0.1132 | 0.0226 | 0.08 | -0.011 |
| 9 | 14.96 | 0.3041 | 0.6608 | -0.2265 | 0.0453 | 0.08 | -0.101 |
| 10 | 15.96 | 0.4155 | 0.6831 | -0.3199 | 0.0640 | 0.08 | -0.176 |
| 11 | 16.96 | 0.4856 | 0.6971 | -0.3815 | 0.0763 | 0.08 | -0.225 |
| 12 | 17.96 | 0.5095 | 0.7019 | -0.4030 | 0.0806 | 0.08 | -0.242 |
| 13 | 18.96 | 0.4856 | 0.6971 | -0.3815 | 0.0763 | 0.08 | -0.225 |
| 14 | 19.96 | 0.4155 | 0.6831 | -0.3199 | 0.0640 | 0.08 | -0.176 |
| 15 | 20.96 | 0.3041 | 0.6608 | -0.2265 | 0.0453 | 0.08 | -0.101 |
| 16 | 21.96 | 0.1589 | 0.6318 | -0.1132 | 0.0226 | 0.08 | -0.011 |
| 17 | 22.96 | 0 | 0.6 | 0 | 0 | 0.08 | 0.080 |
| 18 | 23.96 | 0 | 0.6 | 0 | 0 | 0.08 | 0.080 |
| 19 | 24.96 | 0 | 0.6 | 0 | 0 | 0.08 | 0.080 |
| 20 | 25.96 | 0 | 0.6 | 0 | 0 | 0.08 | 0.080 |
| 21 | 26.96 | 0 | 0.6 | 0 | 0 | 0.08 | 0.080 |
| 22 | 27.96 | 0 | 0.6 | 0 | 0 | 0.08 | 0.080 |
| 23 | 28.96 | 0 | 0.6 | 0 | 0 | 0.08 | 0.080 |
| 24 | 29.96 | 0 | 0.6 | 0 | 0 | 0.08 | 0.080 |

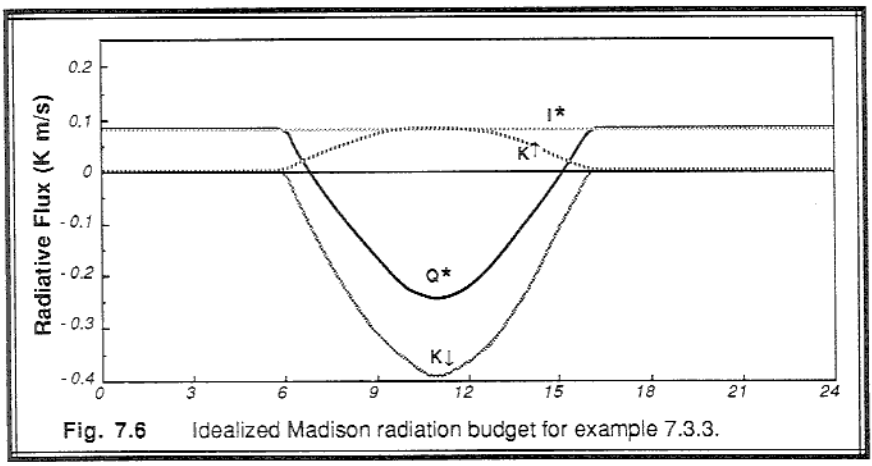


**Fig. 7.6** Idealized Madison radiation budget for example 7.3.3.

**Discussion**: The radiation terms in this equation are plotted in Fig 7.6 for the 24-hour period. As expected, there is net heating during the day and cooling at night. Heating starts almost an hour after sunrise, and ends roughly an hour before sunset.

## 7.4 Fluxes at Interfaces

The vertical flux, $F_\xi$, of any variable $\xi$ is assumed to be driven by the difference in $\overline{\xi}$ across the interface

$$F_\xi = - U_T (\overline{\xi}_{top} - \overline{\xi}_{bottom}) \qquad (7.4a)$$

where $U_T$ represents a ***transport velocity*** across that interface, and the $\overline{\xi}_{top}$ and $\overline{\xi}_{bottom}$ are the values just above and below the boundary. It can also be thought of as a ***conductivity***, because a given $\overline{\xi}$-difference (voltage potential) yields a greater flux (current) if the conductivity is greater.

The transport velocity is usually parameterized as a function of some measure of turbulence appropriate to the type of interface:

$$U_T = C_D \cdot \overline{M} \qquad \text{at } z = 0 \qquad (7.4b)$$

and

$$U_T = w_e \qquad \text{at } z = z_i \qquad (7.4c)$$

where $\overline{M}$ is the mean horizontal wind magnitude at height z above the surface, $C_D$ is the ***bulk transfer coefficient*** for the same height, and $w_e$ is the ***entrainment velocity*** into the top of the mixed layer.

At the surface, the wind speed is zero, while at some height just above the surface there is a nonzero wind. The resulting shear is assumed to generate turbulence which supports the transport. This parameterization obviously fails in calm wind conditions.

The entrainment zone is an interface between the free atmosphere and the mixed layer. Entrainment brings air into the mixed layer from the free atmosphere, and creates a flux just within the top of the mixed layer. Just above the entrainment zone, however, the flux is often near zero, and is unrelated to the entrainment flux just below the entrainment zone interface (see Chapter 11 for more details).

### 7.4.1 Surface Fluxes — Drag and Bulk Transfer Methods

**Definitions.** In 1916, G.I. Taylor suggested that a velocity squared law might be used to describe the drag of the atmosphere against the earth's surface. Using $u_*^2$ as a measure of surface stress associated with drag, we find that

$$u_*^2 = C_D \overline{M}^2 \tag{7.4.1a}$$

For momentum transfer, $C_D$ is called the ***drag coefficient***. Generically it is still a bulk transfer coefficient, and sometimes is written as $C_M$ in the literature. The individual components of surface stress are correspondingly given by the ***drag laws***:

$$(\overline{u'w'})_s = - C_D \overline{M}\,\overline{U} \tag{7.4.1b}$$

$$(\overline{v'w'})_s = - C_D \overline{M}\,\overline{V} \tag{7.4.1c}$$

At first glance (7.4.1b) does not appear to follow the form of (7.4a), but it turns out that the proper form is followed because the wind speed below the surface is zero. Thus, $\overline{U} = \overline{U} - 0 = \overline{U}_{air} - \overline{U}_{ground} = \overline{U}_{top} - \overline{U}_{bottom}$. The three factors $C_D$, $\overline{M}$ and $\overline{U}$ should all correspond to the same height above the surface. Often 10 m is assumed as the standard height, if not otherwise specified.

Similar expressions can be used to parameterize surface heat and moisture fluxes:

$$(\overline{w'\theta'})_s = - C_H \overline{M}\,(\overline{\theta} - \theta_G) \tag{7.4.1d}$$

$$(\overline{w'q'})_s = - C_E \overline{M}\,(\overline{q} - q_G) \tag{7.4.1e}$$

where the subscript $_G$ denotes "on the ground or sea surface".

The parameters $C_H$ and $C_E$ are the ***bulk transfer coefficients*** for heat and moisture, respectively, although sometimes $C_H$ is called the ***Stanton number***. For statically neutral conditions (subscript N), it is often assumed that

$$C_{HN} = C_{EN} = C_{DN} \tag{7.4.1f}$$

Typical values range from $1x10^{-3}$ to $5x10^{-3}$ (dimensionless).

There is a subtle, but important, difference between subscripts $_G$ and $_s$. Subscript $_s$ represents values in the ***air*** near the surface, where "near" often means at 2 m or 10 m above the surface. The subscript $_G$ means the value in the top 1 mm of the soil or sea surface, or sometimes a ***skin*** value representative of just the top few molecules of the soil or sea.

One problem is how to specify the "surface" value, $\theta_G$, or $q_G$. Over the sea, it is often assumed that the air in the micro layer is saturated. The saturation specific humidity is a well known function of temperature (Wallace and Hobbs, 1977). Over land, the soil surface temperature and moisture depend on many factors, and are not easily approximated. One approach is to include forecast equations for the temperature and moisture for a thin layer of soil, such as is described in more detail in section 7.6. Another approach, for temperature, is to radiometrically measure the surface skin temperature (Huband and Monteith, 1986).

**Dependence on Surface Roughness.** Rougher surfaces are likely to cause more intense turbulence, which increases the drag and transfer rates across the surface.

Over land, drag of the air can be caused by frictional skin drag, form drag, and wave drag. ***Frictional skin drag*** is related to the molecular diffusion of momentum across an interface, and applies equally well to transport of heat and scalars. Usually, drag associated with small size obstacles such as blades of grass or gravel or sometimes even trees are parameterized as skin drag in the atmosphere. ***Form drag*** is related to the dynamic pressure differential formed by the deceleration of air as it hits an obstacle such as a mountain or a building. There is no analogy to form drag for heat or scalars. ***Wave drag*** is related to the transport of momentum by buoyancy (gravity) waves in statically stable air. Mountain waves are a classic example.

Since waves and pressure fluctuations can transport momentum but not heat or scalars, we see that the momentum drag coefficient could be significantly different in magnitude from the bulk transfer coefficients for heat or moisture. Thus, one should be cautious when equating transfer coefficients.

When averaged over large horizontal regions such as continents, all drag processes can contribute. Table 7-2 indicates the magnitude such drag coefficients.

**Table 7-2.** Average values of drag coefficients ($C_{DN}$, for 10 m winds) over continents for neutral stability. Geostrophic drag coefficients ($C_{GN}$) for neutral stability over continents. After Garratt (1977).

| Continent | $C_{DN}$ | $C_{GN}$ |
|---|---|---|
| North America | $10.1 \times 10^{-3}$ | $1.89 \times 10^{-3}$ |
| South America | $26.6 \times 10^{-3}$ | $2.16 \times 10^{-3}$ |
| Northern Africa | $2.7 \times 10^{-3}$ | $1.03 \times 10^{-3}$ |
| Southern Africa | $12.9 \times 10^{-3}$ | $1.98 \times 10^{-3}$ |
| Europe | $6.8 \times 10^{-3}$ | $1.73 \times 10^{-3}$ |
| U.S.S.R. | $7.9 \times 10^{-3}$ | $1.83 \times 10^{-3}$ |
| Asia (north of 20°N) | $3.9 \times 10^{-3}$ | $1.31 \times 10^{-3}$ |
| Asia (south of 20°N) | $27.7 \times 10^{-3}$ | $2.18 \times 10^{-3}$ |
| Australia | $6.0 \times 10^{-3}$ | $1.50 \times 10^{-3}$ |

On a smaller scale, one measure of roughness is the spacing density of individual obstacles or ***roughness elements***. For example, the leaves of many trees, plants, and crops can form a ***canopy*** elevated above the ground surface. If we imagine that a large box could be placed over one whole plant or tree that would just touch the top and sides of the plant, then the volume of this box represents the ***space*** taken by the plant. Of course, most of this space is filled by air between the leaves and branches. The total surface area of the plant, including the area of both sides of each leaf can theoretically be measured or estimated. The ***area density of roughness elements***, $S_r$, is defined as the plant surface-area divided by the space volume. A ***dimensionless canopy density***, $C_*$, can be defined by:

$$C_* = c_m S_r h^* \qquad (7.4.1g)$$

where $c_m$ is the drag coefficient associated with an individual roughness element ($c_m$ = 0.05 to 0.5 for typical plants and crops), and $h^*$ is the average height of the canopy (Kondo and Kawanaka, 1986).

The variation of bulk transfer coefficients with canopy density is shown in Fig 7.7. As expected, the value of the transfer coefficients increase as the canopy density increases, corresponding to more roughness elements. For dimensionless canopy densities greater than about 0.4 to 1.0, however, the bulk transfer coefficients decrease. This happens when the roughness elements are so close together that they begin to appear to the wind as a solid smooth surface displaced above the true ground.

Another measure of the surface roughness is the ***aerodynamic roughness length***, $z_o$, which will be discussed in more detail in Chapter 9. It is on the order of centimeters over grass and crops, and on the order of meters over sparse forests and

towns. This roughness measure is based on the observed wind shear in the surface layer, and thus avoids the necessity of estimating the areas and spaces occupied by each roughness element.

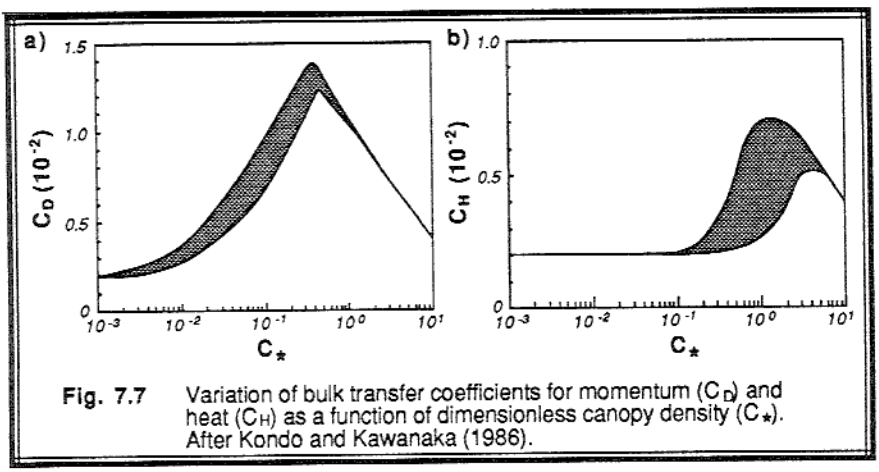


**Fig. 7.7** Variation of bulk transfer coefficients for momentum ($C_D$) and heat ($C_H$) as a function of dimensionless canopy density ($C_*$). After Kondo and Kawanaka (1986).

Over oceans, the drag laws are a bit easier to parameterize, because the roughness length associated with ocean wave height is a known function of surface stress or wind speed:

$$z_o = 0.015 \frac{u_*^2}{g} \qquad (7.4.1h)$$

which is known as ***Charnock's relation*** (1955). Stronger wind stress make higher waves, which results in a greater roughness length. The application of roughness length to bulk transfer is tied to the topic of measurement heights, which is discussed next.

**Dependence on Measurement Height.** As introduced earlier, the factors $C_H$, $\overline{M}$ and $\overline{\theta}$ should all correspond to the same heights, z, above the surface. Unfortunately, no standard has been set on which height to use. One obvious height is instrument shelter height. A problem is that "surface" temperature and moisture are routinely measured at z = 2 m, while "surface" winds are measured at z = 10 m. In numerical models, an obvious height would be the height of the lowest grid point, even though it may be hundreds of meters above the surface. The height used has a dramatic affect on the value of the drag coefficient, because the wind speed and the difference between surface and elevated values of temperature or humidity increase as height increases for any given surface flux. This requires that magnitude of the bulk transfer coefficient decreases with height z to yield the proper surface flux.

The relationship between drag coefficient, measurement height, and surface roughness under statically ***neutral*** conditions in the surface layer over either land or oceans is given by:

$$C_{DN} = k^2 \left[ \ln\left(\frac{z}{z_o}\right) \right]^{-2} \qquad (7.4.1i)$$

This can be derived from the log-wind profile, which is reviewed in Chapter 9.

For oceans, (7.4.1i) can be combined with Charnock's relationship to give:

$$C_{DN} = 4.4 \times 10^{-4}\, \overline{M}^{\,0.55} \qquad (7.4.1j)$$

which yields a surface stress of:

$$u_*^2 = 4.4 \times 10^{-4}\, \overline{M}^{\,2.55} \qquad (7.4.1k)$$

Fig 7.8 shows how these relationships compare to observations of stress and drag over the oceans and over ice. Occasionally, numerical modelers use constant drag values for simplicity, such as the value of $C_{DN} = 1.5 \times 10^{-3}$ based on 10 m winds suggested by Anthes & Keyser (1979).

Typical values for $C_{DN}$ and $C_D$ over land are listed in Table 7-3.

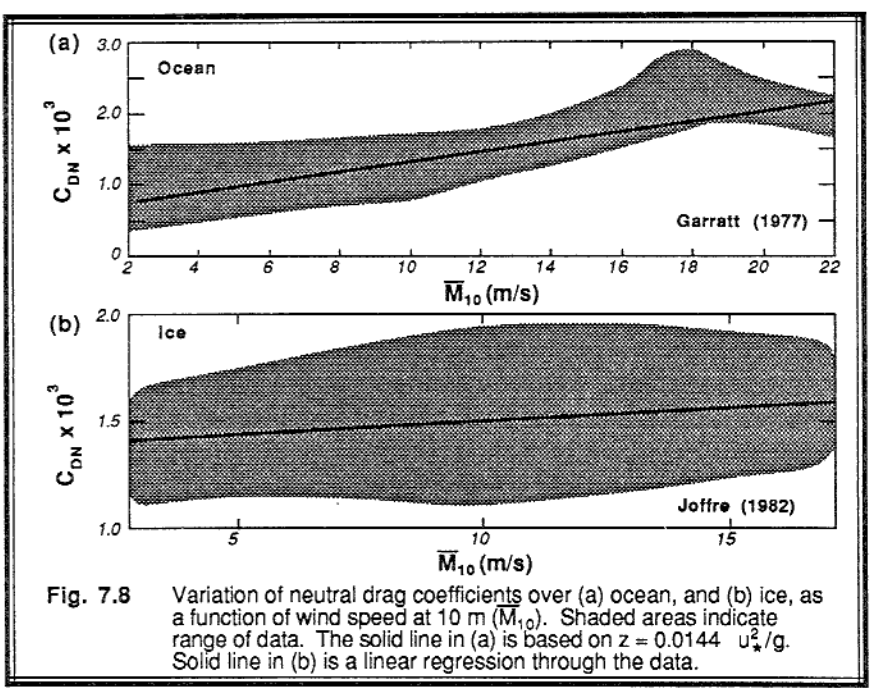


**Fig. 7.8** Variation of neutral drag coefficients over (a) ocean, and (b) ice, as a function of wind speed at 10 m ($\overline{M}_{10}$). Shaded areas indicate range of data. The solid line in (a) is based on $z = 0.0144\ u_*^2/g$. Solid line in (b) is a linear regression through the data.

**Table 7-3.** Sample drag and bulk-transfer coefficients. After Garratt (1977), Anthes and Keyser (1979), Gadd and Keers (1970), Deardorff (1968), Verma, et al. (1986), and Kondo and Yamazawa (1986a).

| Coefficient | Ratio | Conditions |
|---|---|---|
| $C_{DN} = 2.6 \times 10^{-3}$ | | 10 m winds over plains, nighttime |
| $C_D = 1.3$ to $1.5 \times 10^{-3}$ | $C_D / C_{DN} = 0.5$ | 10 m winds over plains, nighttime |
| $C_{DN} = 1.4 \times 10^{-3}$ | | 10 m winds over plains, daytime |
| $C_D = 1.8 \times 10^{-3}$ | $C_D / C_{DN} = 1.3$ | 10 m winds over plains, dayttime |
| $C_D = 16.0 \times 10^{-3}$ | | 10 m winds over deciduous forest |
| $C_D = 40.0$ to $160.0 \times 10^{-3}$ | | 10 m winds over coniferous forest |
| $C_H = 2.0 \times 10^{-3}$ | | 10 m winds over snow surface |
| $C_D = [k^{-1} \cdot \ln(u_* z / \nu) + 5.5]^{-2}$ | | 10 m winds over snow surface |
| $C_D = 5.0 \times 10^{-3} + (6.45 \times 10^{-3}) \cdot [z_T/(1+z_T)]$ | | for $z_T$ = terrain height in km |
| $C_D = [1 + 2.5 \cdot z_T] \times 10^{-3}$ | | for $z_T$ = terrain height in km |
| $C_{DN} = [1 + 0.07 \cdot M] \times 10^{-3}$ | | 10 m winds over plains, nighttime |
| $C_{DN} = [0.75 + 0.067 \cdot M] \times 10^{-3}$ | | 10 m winds over water |
| $C_{DN} = [1 + 0.07 \cdot M] \times 10^{-3}$ | | 10 m winds over water |
| $C_D = 0.7 \times 10^{-3}$ | | 10 m winds over water |
| $C_{DN} = 0.51 \times 10^{-3} \cdot M^{0.46}$ | | 10 m winds over water |

**Dependence on Stability.** Statically unstable flows generally cause a greater transport rate across an interface than statically neutral flows, which in turn transport more than stable flows. Sometimes Richardson numbers are used as a measure of stability, while at other times $\zeta = z/L$ is used. The dimensionless wind shear, $\phi_M(\zeta)$, and lapse rate, $\phi_H(\zeta)$, can be used with surface-layer similarity theory (to be described in Chapter 9) to give stability correction terms [$\psi_M(\zeta)$ and $\psi_H(\zeta)$]. This yields:

$$C_D = k^2 \left[ \ln\left(\frac{z}{z_o}\right) - \psi_M(\zeta) \right]^{-2} \tag{7.4.1l}$$

$$C_H = k^2 \left[ \ln\left(\frac{z}{z_o}\right) - \psi_M(\zeta) \right]^{-1} \left[ \ln\left(\frac{z}{z_o}\right) - \psi_H(\zeta) \right]^{-1} \tag{7.4.1m}$$

It is usually assumed that $C_E = C_H$. Figs 7.9 and 7.10, based on the work of Louis (1979), Garratt (1977), Joffre (1982) and Greenhut (1982), show the variation of bulk transfer coefficients with stability, sensor height, and roughness.

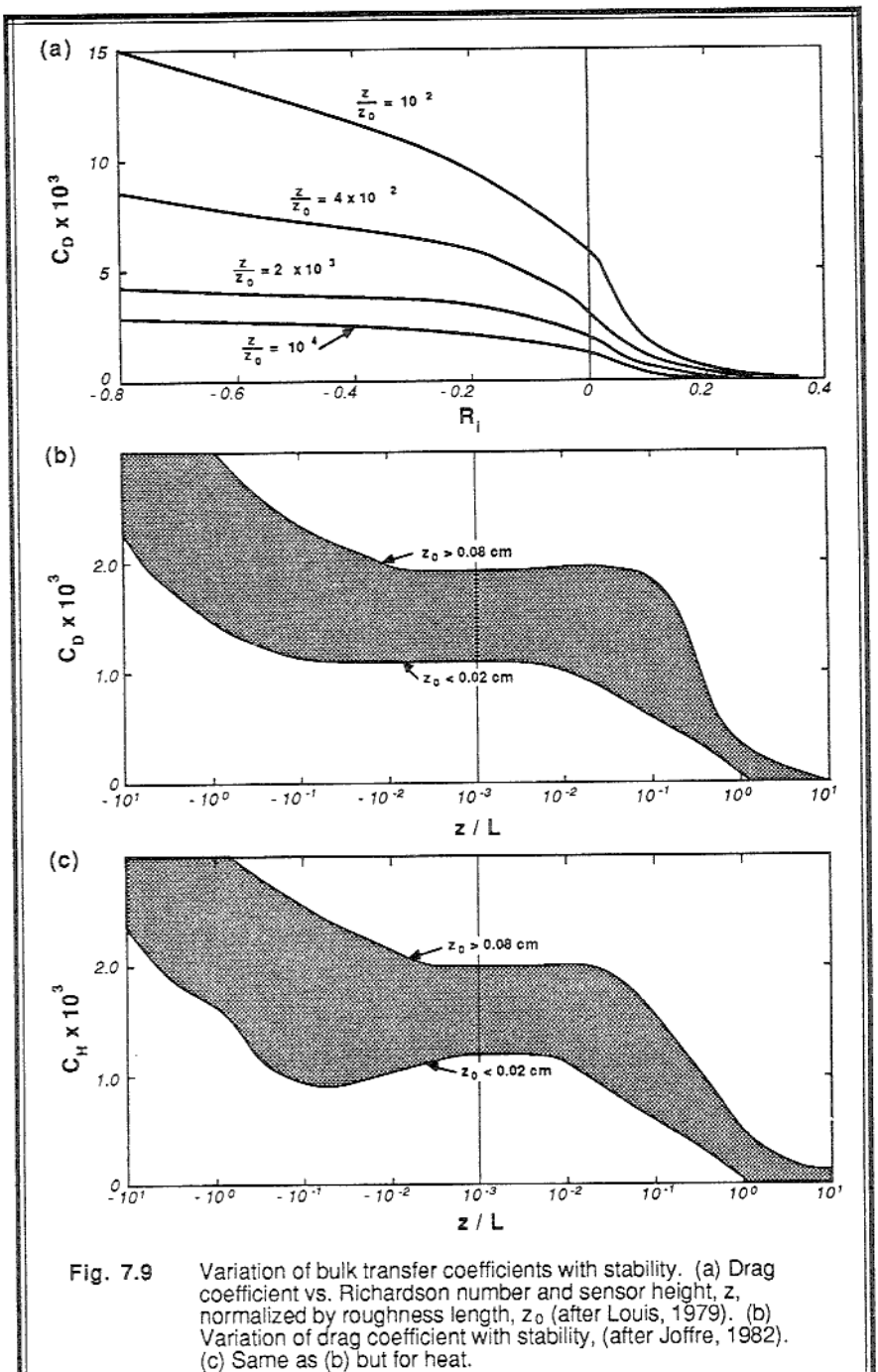


Fig. 7.9 Variation of bulk transfer coefficients with stability. (a) Drag coefficient vs. Richardson number and sensor height, z, normalized by roughness length, $z_0$ (after Louis, 1979). (b) Variation of drag coefficient with stability, (after Joffre, 1982). (c) Same as (b) but for heat.

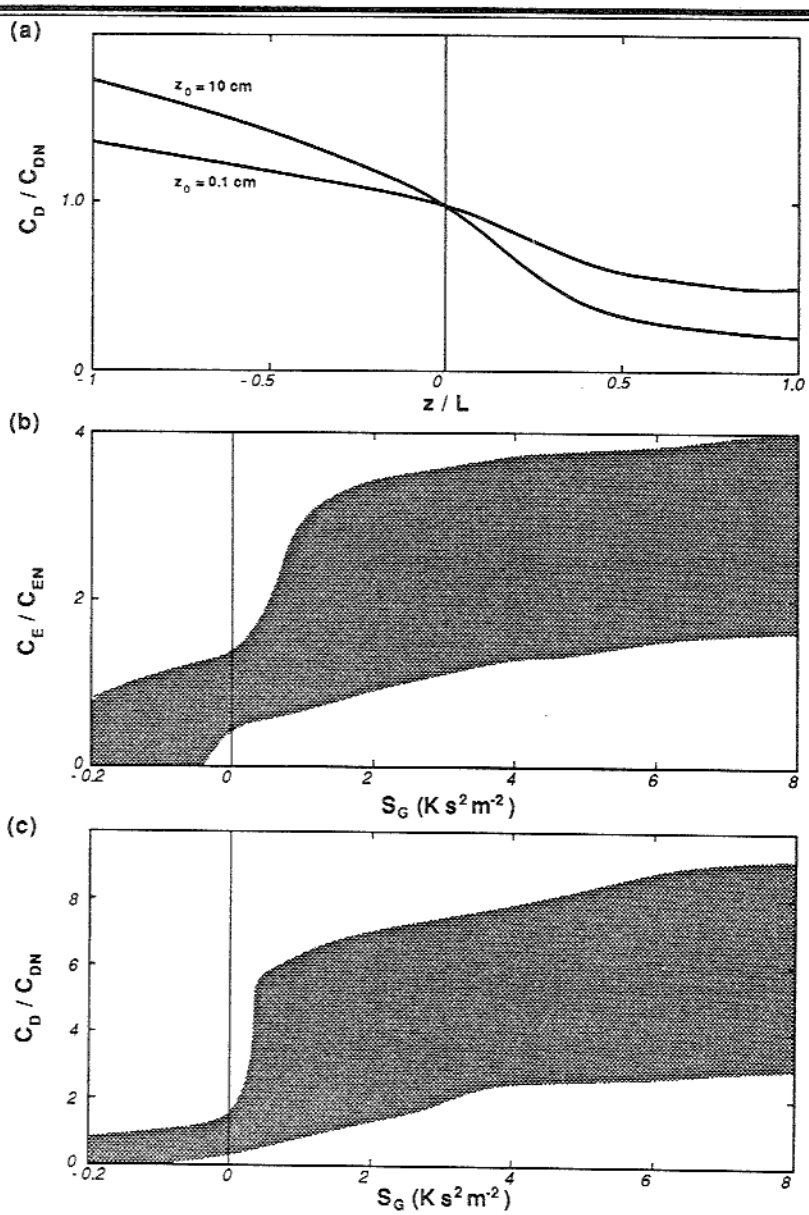


**Fig. 7.10** Ratio of bulk transfer coefficients to their neutral values. (a) Comparison of diabatic to neutral drag coefficients as a function of roughness length and stability, z/L (after Garratt, 1977). (b) Ratio of diabatic to neutral bulk transfer coefficient for moisture as a function of stability, $s_G = (\theta_s - \theta_{air}) / M^2 [1 + \log \frac{z_0}{z})]^2$ (after Greenhut, 1982). Shaded regions indicate the range of observed data. (c) Same as (b) but for momentum.

**7.4.2 Surface Fluxes — Geostrophic Drag.** Sometimes in numerical or theoretical models, one does not know the winds anywhere near the surface, but one can calculate the geostrophic wind instead. Deacon (1973), Clarke and Hesse (1974), Melgargejo and Deardorff (1974), Arya (1975), Nicholls (1982), and Grant and Whiteford (1987) parameterized surface fluxes in terms of geostrophic wind, using

$$F_\xi = - C_G \, \overline{G} \left( \overline{\xi}_{top} - \overline{\xi}_{bottom} \right) \tag{7.4.2a}$$

where $\overline{G}$ is the magnitude of the geostrophic wind, and $C_G$ is called the ***geostrophic drag coefficient***. This parameterization is usually not as accurate as the one using surface wind, and should be avoided unless you have no choice.

Typical magnitudes of $C_G$ were given in Table 7-2 for continental areas. Table 7-4 lists suggested values over other areas. Although we are defining geostrophic drag based on $u_*^2 = C_G \, G^2$, some investigators use $u_* = C_G \, G$ instead. Be careful to check which definition is used for $C_G$ when comparing values reported in the literature.

One parameterization for the neutral geostrophic drag coefficient is

$$C_{GN} = 0.0123 \, Ro^{-0.14} \tag{7.4.2b}$$

where $Ro = \overline{G}/(f_c \, z_o)$ is the ***surface Rossby number***. Its variation with stability is given in Fig 7.11.

**Table 7-4.** Typical values of geostrophic drag coefficients ($C_{GN}$) for neutral stability over a variety of surfaces. After Garratt (1977), Grant and Whiteford (1987), and Kondo and Yamazawa (1986).

| Surface | $C_{GN}$ |
|---|---|
| sea | $0.73 \times 10^{-3}$ |
| rice paddies | $1.1 \times 10^{-3}$ |
| plains | $2.2 \times 10^{-3}$ |
| sparse houses or trees | $2.0$ to $2.5 \times 10^{-3}$ |
| low mountains | $2.5$ to $2.7 \times 10^{-3}$ |
| cities with tall buildings | $2.7 \times 10^{-3}$ |
| moderately high mountains | $3$ to $5 \times 10^{-3}$ |
| very high mountains | $8$ to $10 \times 10^{-3}$ |

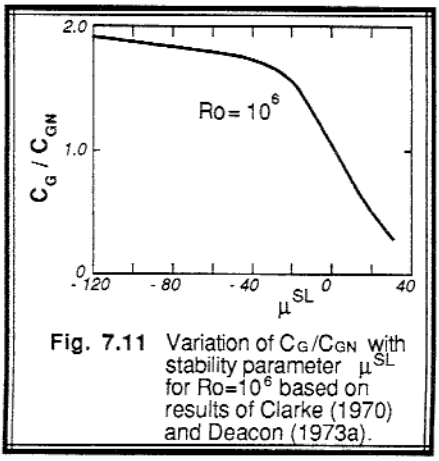


**Fig. 7.11** Variation of $C_G/C_{GN}$ with stability parameter $\mu^{SL}$ for Ro=$10^6$ based on results of Clarke (1970) and Deacon (1973a).

Over oceans, Charnock's relationship gives (for geostrophic winds in m/s):

$$C_{GN} = 4.4 \times 10^{-4}\ \overline{G}^{\,0.16} \qquad (7.4.2c)$$

$$u_*^2 = 4.8 \times 10^{-4}\ \overline{G}^{\,2.16} \qquad \text{(at 45°N)} \qquad (7.4.2d)$$

### 7.4.3 Entrainment into the Top of the Mixed Layer

The top of the mixed layer sometimes behaves like a boundary, where the fluxes across it are controlled by the entrainment mechanism. When (7.4a) and (7.4c) are combined with the definition that $\Delta\xi = [\ \xi|_{\text{just above ML top}} - \xi|_{\text{within ML}}\ ]$, then:

$$F_\xi = \overline{w'\xi'} = -w_e\ \Delta\overline{\xi} \qquad (7.4.3a)$$

This expression can also be derived from Leibniz' theorem (see section 2.4.2). Using the mixing ratio example from that section (where $z_i^+$ denotes the value just above $z_i$)

$$\frac{d\left[z_i\,\bar{r}\right]}{dt} = z_i\left[\frac{\overline{\partial r}}{\partial t}\right] + r\left(t, z_i^+\right)\ \frac{dz_i}{dt}$$

The left hand side can be rewritten using the product rule of calculus as $\bar{r}\ dz_i/dt + z_i\ d\bar{r}/dt$, where $\bar{r}$ represents an average within the mixed layer. Combining the first term from this

expansion with the last term on the right hand side, and dividing by $z_i$ gives:

$$\frac{d\bar{r}}{dt} = \left[\overline{\frac{\partial r}{\partial t}}\right] + \frac{w_e \Delta \bar{r}}{z_i} \qquad (7.4.3b)$$

using $w_e = d\, z_i/dt$ (in the absence of subsidence or clouds) and $\Delta\bar{r} = \bar{r}(t,z_i^+) - \bar{r}$.

But from (3.5.3) we know that the change in moisture in the mixed layer $d\bar{r}/dt$ is caused by various sources and sinks, $[\overline{\partial r/\partial t}]$, including flux divergence of surface flux and the flux divergence $\partial F/\partial z = F_{top}/z_i$ of flux from the top of the mixed layer. Hence:

$$\frac{d\bar{r}}{dt} = \left[\overline{\frac{\partial r}{\partial t}}\right] + \frac{\left[F_{top}\right]}{z_i} \qquad (7.4.3c)$$

Comparing (7.4.3b) and (7.4.3c), we conclude that $F_{top} = \overline{w'r'}|_{z_i} = -w_e\Delta\bar{r}$ . One must remember that this interfacial flux occurs only when there is turbulent entrainment of air across the capping interface.

## 7.5 Partitioning of Flux into Sensible and Latent Portions

One alternative to the detailed modeling of surface temperature and soil moisture, as used in the previous section to find the heat, moisture, and momentum fluxes, is direct partitioning of the incoming solar radiative flux, described next.

Over land in clear-sky situations with weak or no advection, the fluxes of sensible and latent heat from the surface are governed by the diurnal cycle of solar radiation. Consider, for example, a situation where initially the sun is turned off, and the ground and air are at the same temperature. After turning on the sun with a constant net radiation of $Q^*$, the surface will warm. As it warms, a sensible heat flux will develop to remove some of the excess heat from the ground surface to the air. If the ground is moist, evaporation will also remove heat. Some heat will also be conducted into the ground.

If the removal of heat by sensible, latent, and ground fluxes is insufficient to balance the incoming $Q^*$, then the surface temperature will continue to warm. As it does, the sensible, latent, and ground fluxes will also increase until an equilibrium condition is finally reached where incoming radiative flux is balanced by outgoing turbulent and molecular fluxes. Although the surface temperature is important in creating this equilibrium, at equilibrium the fluxes must balance regardless of that temperature.

This argument suggests a parameterization where the net incoming radiation can be split or partitioned directly into the other fluxes of sensible, latent, and ground flux as governed by (7.2c), without requiring a forecast of ground surface temperature. In other words, the incoming radiation is an external forcing, while the sensible ($Q_H$), latent ($Q_E$) and ground fluxes ($Q_G$) are the response. The flux into the ground is often a small, but

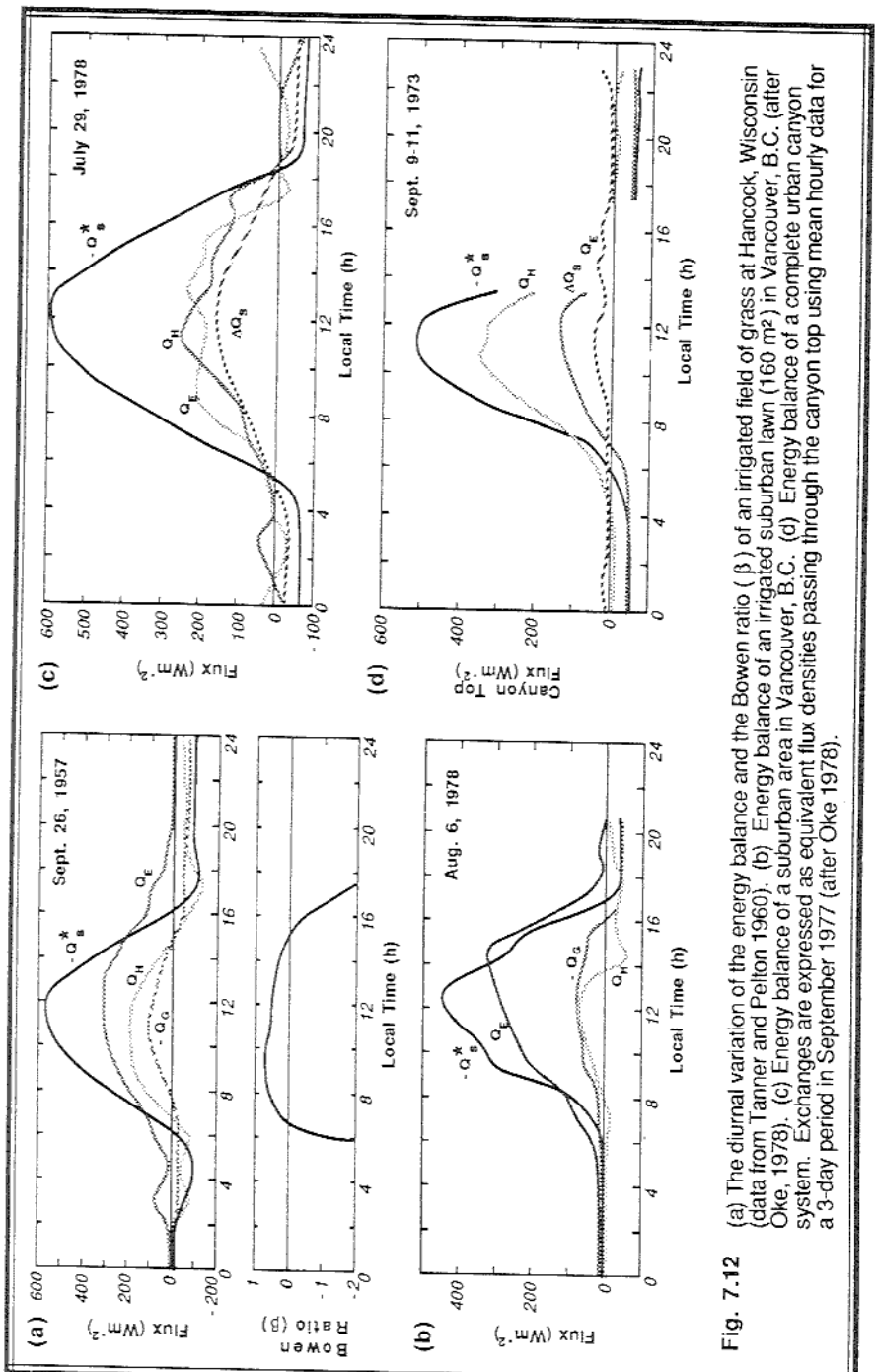


Fig. 7.12 (a) The diurnal variation of the energy balance and the Bowen ratio ( β ) of an irrigated field of grass at Hancock, Wisconsin (data from Tanner and Pelton 1960). (b) Energy balance of an irrigated suburban lawn (160 m²) in Vancouver, B.C. (after Oke, 1978). (c) Energy balance of a suburban area in Vancouver, B.C. (d) Energy balance of a complete urban canyon system. Exchanges are expressed as equivalent flux densities passing through the canyon top using mean hourly data for a 3-day period in September 1977 (after Oke 1978).

not negligible, fraction of the net radiation, as will be discussed in section 7.6. For now, we will treat $(-Q^*_s + Q_G)$ as the imposed forcing, which must be partitioned into $Q_H$ and $Q_E$:

$$(-Q^*_s + Q_G) = Q_H + Q_E \tag{7.5}$$

As we saw in Fig. 7.4, both $Q_H$ and $Q_E$ reach a peak during midday at roughly the same time as the solar forcing peaks, and are small in the morning and evening. This supports our idea of partitioning. However, a close examination of similar budget data from other sites (Fig. 7.12) suggests that the relative magnitudes of $Q_H$ and $Q_E$ vary depending on the wetness and vegetation of the surface. Any parameterization should take this variation into account.

### 7.5.1 Bowen Ratio Methods

The ***Bowen ratio***, $\beta$, is defined as the ratio of sensible to latent heat fluxes at the surface:

$$\beta = \frac{Q_H}{Q_E} = \frac{\left(c_p \overline{w'\theta'_s}\right)}{\left(L_v \overline{w'q'_s}\right)} = \frac{\gamma \overline{w'\theta'_s}}{\overline{w'q'_s}} \tag{7.5.1a}$$

where $\gamma = C_p/L_v \cong 0.0004\ (g_{water}/g_{air})\cdot K^{-1}$ is the ***psychrometric constant***. As one might expect, $\beta$ is smaller over moist surfaces where most of the energy goes into evaporation, and larger over dry surfaces where most of the energy goes into sensible heating. Typical values range from 5 over semi-arid regions, 0.5 over grasslands and forests, 0.2 over irigated orchards or grass, 0.1 over the sea, to some negative values over oases.

It was once suggested that if the Bowen ratio for a surface were known, then (7.5.1a) could be coupled with (7.5) to give:

$$Q_H = \frac{\beta\,(-Q^*_s + Q_G)}{(1+\beta)} \tag{7.5.1b}$$

$$Q_E = \frac{(-Q^*_s + Q_G)}{(1+\beta)} \tag{7.5.1c}$$

Attempts to use this approach have mostly failed, because the Bowen ratio usually varies with time and weather over each site. Furthermore, the ***evapotranspiration*** component of latent heat flux from plants is a complex function of the age, health, temperature and water stress of the plant. The pores, or stomates, of the plant open and close to regulate the life processes of the plant. Thus, the ***stomatel resistance*** to water flux, or transpiration, also varies.

### 7.5.2 Priestley-Taylor Method

The next level of sophistication (Priestley and Taylor, 1972) comes by recognizing that to first order, we can use K-theory to approximate the fluxes by gradients of temperature and humidity in the Bowen ratio, assuming that $K_E = K_H$:

$$\beta = \gamma \frac{\partial \bar{\theta} / \partial z}{\partial \bar{q} / \partial z} = \frac{\left[ \gamma \left( \partial \bar{T} / \partial z + \Gamma_d \right) \right]}{\partial \bar{q} / \partial z} \qquad (7.5.2a)$$

where $\Gamma_d$ is the dry adiabatic lapse rate of 9.8 K/km. If the air is saturated (i.e., if $q = q_{sat}$), then the change of specific humidity with temperature is given by the ***Clausius-Clapeyron*** equation:

$$\frac{dq_{sat}}{dT} = \frac{\varepsilon L_v \bar{q}_{sat}}{(\Re \bar{T}^2)} \equiv s_{cc}(\bar{T}) \qquad (7.5.2b)$$

where $\varepsilon = 0.622 \, (g_{water} / g_{air})$ is the ratio of gas constants for air and water vapor.

We can use a variation of Teten's formula (Bolton, 1980) to find $q_{sat}$ as a function of temperature (Fig. 7.13):

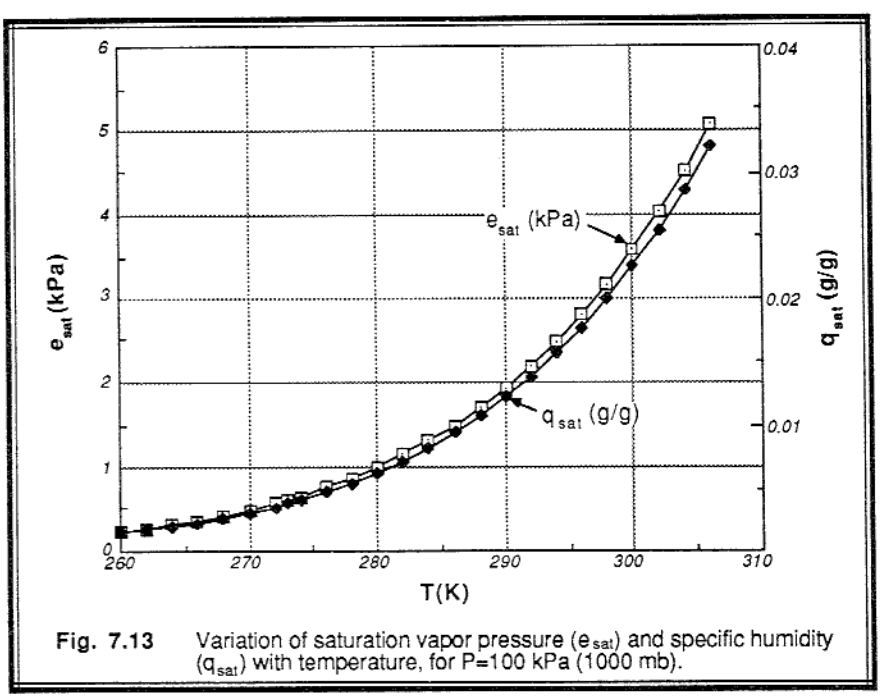


**Fig. 7.13** Variation of saturation vapor pressure ($e_{sat}$) and specific humidity ($q_{sat}$) with temperature, for P=100 kPa (1000 mb).

$$q_{sat} = 0.622 \frac{e_{sat}}{P} \tag{7.5.2c}$$

where:

$$e_{sat} = (0.6112\ \text{kPa}) \cdot \exp\left[\frac{17.67 \cdot (T - 273.16)}{T - 29.66}\right] \tag{7.5.2d}$$

for T in degrees Kelvin.

Both $s_{cc}(\overline{T})$ and $\gamma(\overline{T}) = C_p/L_v$ are plotted in Fig. 7.14 for easy reference. If we replace $\partial\overline{q}/\partial z$ by $s_{cc}(\overline{T}) \cdot \partial\overline{T}/\partial z$, then:

$$\beta = \frac{\left[\gamma\,(\partial\overline{T}/\partial z + \Gamma_d)\right]}{(s_{cc}\,\partial\overline{T}/\partial z)} \tag{7.5.2e}$$

or

$$\beta = \frac{\gamma}{s_{cc}} + \frac{\gamma \cdot \Gamma_d}{s_{cc} \cdot (\partial\overline{T}/\partial z)} \tag{7.5.2f}$$

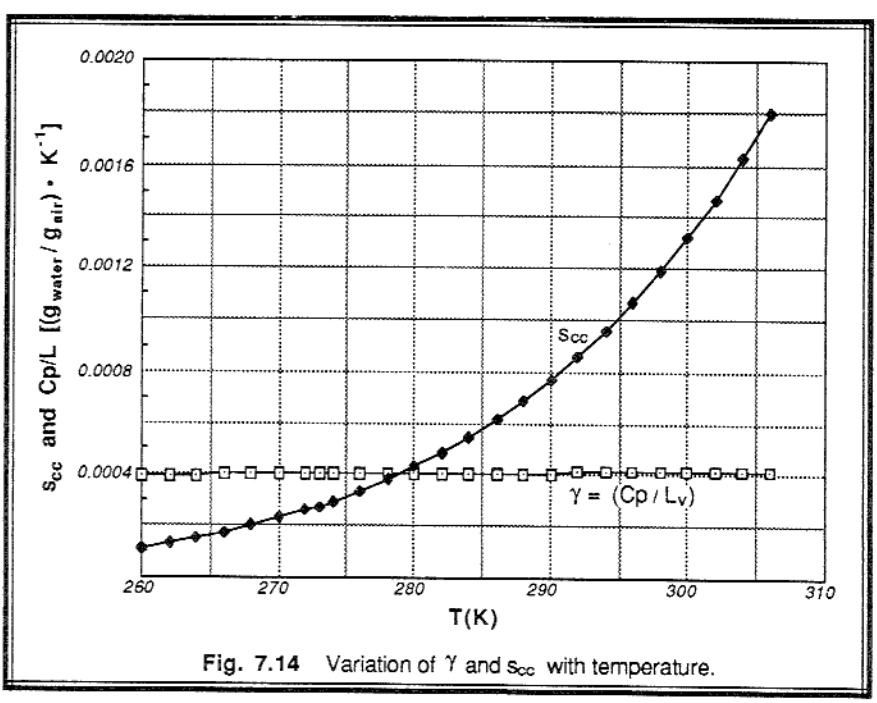


**Fig. 7.14** Variation of $\gamma$ and $s_{cc}$ with temperature.

If one neglects the last term in (7.5.2f), then substitution of (7.5.2f) back into (7.5.1b & c) yields the ***Priestly-Taylor*** parameterization:

$$Q_H = \frac{\left[(1 - \alpha_{PT})\, s_{cc} + \gamma\right]\left(- Q^*_s + Q_G\right)}{(s_{cc} + \gamma)} \qquad (7.5.2g)$$

$$Q_E = \alpha_{PT}\, s_{cc} \frac{(- Q^*_s + Q_G)}{(s_{cc} + \gamma)} \qquad (7.5.2h)$$

where the parameter $\alpha_{PT}$ is introduced to make up for neglecting the last term in (7.5.2f), and to allow the equations to be used for unsaturated conditions (DeBruin and Keijamn, 1979; DeBruin, 1983). For well-watered surfaces, $\alpha_{PT} \cong 1.25$.

The Priestley-Taylor method can yield incorrect fluxes when advection is happening. Although one possible fix is to increase the magnitude of $\alpha_{PT}$ , many investigators (McNaughton, 1976a & b; Singh and Taillefer, 1986) prefer to add an additional advection term, A, to the moisture flux equation to yield: $Q_E = [s_{cc}/(s_{cc}+\gamma)]\cdot(-Q^*_s + Q_G) + A$. This same advection term must be subtracted from the equation for heat flux.

### 7.5.3 Penman-Monteith Method

One way to include the evaporative cooling effects such as occurs during advection is via a correction term, $F_w$, added to the Priestly-Taylor parameterization for $Q_E$ and subtracted from that for $Q_H$ , to yield the ***Penman-Monteith*** (Penman, 1948; Monteith, 1965; deBruin and Holtslag, 1982) form:

$$Q_H = \frac{\left[\gamma(- Q^*_s + Q_G) - F_W\right]}{(X_G\, s_{cc} + \gamma)} \qquad (7.5.3a)$$

$$Q_E = \frac{\left[X_G\, s_{cc}(- Q^*_s + Q_G) + F_W\right]}{(X_G\, s_{cc} + \gamma)} \qquad (7.5.3b)$$

where $X_G$ is like a relative humidity of the earth or plant surface. $F_w$ is like a specific humidity flux, and is approximated by a bulk transfer law of the form: $F_w = C_E \overline{M}\, (X_G - X_s)\cdot\bar{q}_{sat}$ , where $X_s$ is the relative humidity of the air near the surface.

Remembering that $C_E\overline{M}$ is like a conductance for moisture, we see that surfaces with greater water conductivity have a greater latent heat flux and smaller sensible heat flux than less conductive surfaces.

Alternately, we can view the parameterization via the concept of a resistance to transfer. Physically, we would expect that surface/plant systems with less resistance to moisture transport would have greater evaporation, with the resulting reduction in sensible heat flux. For example, the ***air resistance*** , $r_a$, to transfer of water vapor away from a plant stomate into the air is just the inverse of the ***conductance*** ($C_E\overline{M}$) introduced earlier:

$$r_a = 1 / (C_E\overline{M})$$

The total resistance of the plant, $r_p$, is governed by the movement of water from the ground through the roots up into the plant to the cavity of the stomate where it is finally transpired into the air. We can combine the air and plant resistances to rewrite the correction term as: $F_w = (\overline{q}_{sat} - \overline{q}_{air}) / (r_a + r_p)$, where $\overline{q}_{air} = (X_s/X_G)\,\overline{q}_{sat}$ , and $X_G = r_a/(r_a+r_p)$. This expression for $F_w$ is equivalent to the one written earlier.

The topic of fluxes across vegetation systems is a complex one that we have barely parameterized above. A more detailed analysis should include factors such as canopy height, vegetation coverage, displacement heights, roughness lengths, plant reflectivity, plant architecture, root zone depth, ground water depth, heat conductivity, soil moisture, and stomatel resistance. These topics are beyond the scope of this book (see Verma, et al., 1986; Brutsaert, 1985; Mahrt and Ek, 1984; McNaughton and Jarvis, 1983; Deardorff, 1978; Geiger, 1965).

### 7.5.4 Flux Partitioning Example

**Problem**: Find $Q_H$ and $Q_E$ as a function of time for the same situation as presented in the radiation budget example of section 7.3.3. Compare the results of the Priestley-Taylor and the Penman-Monteith methods, given the typical diurnal cycle in temperature as listed in Table 7-5.

Let the surface pressure be constant at 100 kPa (1000 mb). For the first method, assume that $\alpha_{PT} = 1.25$, with no additional advection term. For the second method assume that $C_E = 0.002$, $X_s = 0.5$, $X_G = 0.9$, and $\overline{M} = 5$ m/s.

**Solution**: As in the radiation example, we will employ spreadsheet software to implement the solution. To find the imposed forcing ($-Q^*_s + Q_G$), we can use $Q^*$ from the previous example, but we have not yet discussed parameterizations for $Q_G$. Assume for simplicity that $Q_G = 0.5\ Q^*$ during nighttime, and $Q_G = 0.1\ Q^*$ during the daytime (to be discussed in section 7.6.1). The latent heat of vaporization is approximated by a linear

function of temperature: $L_v(J/kg) = [2.501 - 0.00237 \cdot T(°C)]\ 10^6$. The specific heat at constant pressure is assumed to be constant $C_p = 1005$ J/(kg K), and the gas constant for air is also assumed to be constant $\Re = 287.04$ J/(kg K).

Both the Priestley-Taylor and the Penman-Monteith methods are a function of $s_{cc}$, which in turn is a function of temperature. Table 7-5 lists the values of $L_v(T)$ , $\gamma(T)$, $q_{sat}(T)$, $s_{cc}(T)$, and $(-Q^*_s + Q_G)$, and saturation vapor pressure $e_{sat}(T)$.

In the second page of Table 7-5, we finally compute $Q_E$ and $Q_H$ for both the Priestly-Taylor and the Penman-Monteith methods. Also computed in the table are the Bowen ratios for both methods, and the value of $F_w$ $[(g_{water}/g_{air}) \cdot m/s\ ]$ for the Penman-Monteith method.

**Discussion**: Fig 7.15a-c shows the variations of the terms in the surface energy balance for both methods. Fig 7.15a indicates that all of the fluxes are in phase with the radiative forcing for the Priestely-Taylor method. In particular, all of the fluxes cross the zero line at the same times. The latent heat flux is larger than the sensible heat flux for this case. At night, all of the fluxes are negative, including the latent heat flux. This is related to dew or frost.

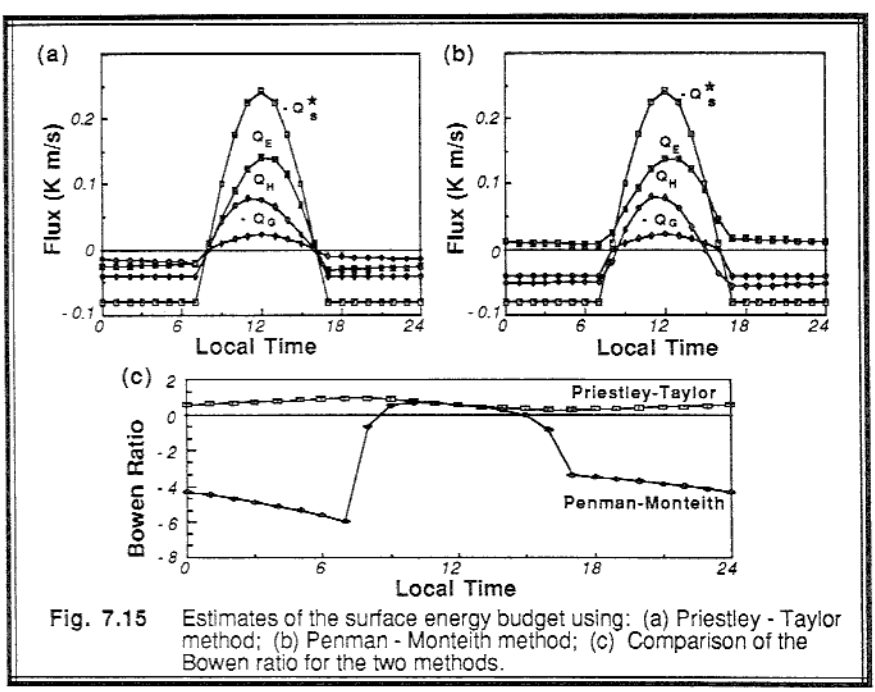


Fig. 7.15 Estimates of the surface energy budget using: (a) Priestley - Taylor method; (b) Penman - Monteith method; (c) Comparison of the Bowen ratio for the two methods.

**Table 7-5.** Flux partitioning example, displayed as output from a spreadsheet.

Flux Partition for: Madison, Wisconsin

P = 1000 mb = 100 kPa
Rv = 287.04 J/(kg K)
Cp = 1005 J/(kg K)

| Local (hr) | Q* (Km/s) | T (K) | Lv (J/kg) | gamma (Cp/Lv) ((g/g)/K) | e sat (mb) | q sat (g/g) | Scc (q/K) | Q*s-QG (K m/s) |
|---|---|---|---|---|---|---|---|---|
| 0 | 0.080 | 280 | 2482500 | 0.00040 | 10.024 | 0.00626 | 0.00043 | 0.040 |
| 1 | 0.080 | 279 | 2485000 | 0.00040 | 9.356 | 0.00584 | 0.00040 | 0.040 |
| 2 | 0.080 | 278 | 2487500 | 0.00040 | 8.728 | 0.00545 | 0.00038 | 0.040 |
| 3 | 0.080 | 277 | 2490000 | 0.00040 | 8.137 | 0.00508 | 0.00036 | 0.040 |
| 4 | 0.080 | 276 | 2492500 | 0.00040 | 7.582 | 0.00473 | 0.00034 | 0.040 |
| 5 | 0.080 | 275 | 2495000 | 0.00040 | 7.060 | 0.00440 | 0.00031 | 0.040 |
| 6 | 0.080 | 274 | 2497500 | 0.00040 | 6.571 | 0.00410 | 0.00030 | 0.040 |
| 7 | 0.080 | 273 | 2500000 | 0.00040 | 6.112 | 0.00381 | 0.00028 | 0.040 |
| 8 | -0.011 | 273 | 2500000 | 0.00040 | 6.112 | 0.00381 | 0.00028 | -0.009 |
| 9 | -0.101 | 274 | 2497500 | 0.00040 | 6.571 | 0.00410 | 0.00030 | -0.091 |
| 10 | -0.176 | 276 | 2492500 | 0.00040 | 7.582 | 0.00473 | 0.00034 | -0.158 |
| 11 | -0.225 | 278 | 2487500 | 0.00040 | 8.728 | 0.00545 | 0.00038 | -0.203 |
| 12 | -0.242 | 280 | 2482500 | 0.00040 | 10.024 | 0.00626 | 0.00043 | -0.218 |
| 13 | -0.225 | 282 | 2477500 | 0.00041 | 11.488 | 0.00718 | 0.00048 | -0.203 |
| 14 | -0.176 | 284 | 2472500 | 0.00041 | 13.138 | 0.00821 | 0.00055 | -0.158 |
| 15 | -0.101 | 286 | 2467500 | 0.00041 | 14.993 | 0.00938 | 0.00061 | -0.091 |
| 16 | -0.011 | 287 | 2465000 | 0.00041 | 16.004 | 0.01001 | 0.00065 | -0.009 |
| 17 | 0.080 | 287 | 2465000 | 0.00041 | 16.004 | 0.01001 | 0.00065 | 0.040 |
| 18 | 0.080 | 286 | 2467500 | 0.00041 | 14.993 | 0.00938 | 0.00061 | 0.040 |
| 19 | 0.080 | 285 | 2470000 | 0.00041 | 14.038 | 0.00878 | 0.00058 | 0.040 |
| 20 | 0.080 | 284 | 2472500 | 0.00041 | 13.138 | 0.00821 | 0.00055 | 0.040 |
| 21 | 0.080 | 283 | 2475000 | 0.00041 | 12.289 | 0.00768 | 0.00051 | 0.040 |
| 22 | 0.080 | 282 | 2477500 | 0.00041 | 11.488 | 0.00718 | 0.00048 | 0.040 |
| 23 | 0.080 | 281 | 2480000 | 0.00041 | 10.734 | 0.00670 | 0.00046 | 0.040 |
| 24 | 0.080 | 280 | 2482500 | 0.00040 | 10.024 | 0.00626 | 0.00043 | 0.040 |

**Table 7-5 (part 2).** Flux partitioning example.

| | | Priestley - Taylor Method | | | | Penman - Monteith Method | | | |
|---|---|---|---|---|---|---|---|---|---|
| | | alpha = 1.25 | | | | CE = 0.002<br>Xa = 0.5<br>Xo = 0.9<br>M(m/s)= 5 | | | |
| time local | Q*s (K m/s) | QG (K m/s) | QE (K m/s) | QH (K m/s) | Bowen Ratio | Fw (g/g)(m/s) | QE (K m/s) | QH (K m/s) | Bowen Ratio |
| 0 | 0.080 | 0.040 | -0.0257 | -0.0143 | 0.554 | 2.5E-05 | 0.0121 | -0.0521 | -4.31 |
| 1 | 0.080 | 0.040 | -0.0250 | -0.0150 | 0.601 | 2.3E-05 | 0.0115 | -0.0515 | -4.48 |
| 2 | 0.080 | 0.040 | -0.0242 | -0.0158 | 0.651 | 2.2E-05 | 0.0109 | -0.0509 | -4.68 |
| 3 | 0.080 | 0.040 | -0.0235 | -0.0165 | 0.704 | 2E-05 | 0.0103 | -0.0503 | -4.89 |
| 4 | 0.080 | 0.040 | -0.0227 | -0.0173 | 0.762 | 1.9E-05 | 0.0097 | -0.0497 | -5.12 |
| 5 | 0.080 | 0.040 | -0.0219 | -0.0181 | 0.824 | 1.8E-05 | 0.0092 | -0.0492 | -5.37 |
| 6 | 0.080 | 0.040 | -0.0212 | -0.0188 | 0.890 | 1.6E-05 | 0.0086 | -0.0486 | -5.64 |
| 7 | 0.080 | 0.040 | -0.0204 | -0.0196 | 0.961 | 1.5E-05 | 0.0081 | -0.0481 | -5.94 |
| 8 | -0.011 | -0.001 | 0.0048 | 0.0046 | 0.961 | 1.5E-05 | 0.0270 | -0.0176 | -0.65 |
| 9 | -0.101 | -0.010 | 0.0482 | 0.0429 | 0.890 | 1.6E-05 | 0.0608 | 0.0303 | 0.50 |
| 10 | -0.176 | -0.018 | 0.0899 | 0.0685 | 0.762 | 1.9E-05 | 0.0946 | 0.0637 | 0.67 |
| 11 | -0.225 | -0.023 | 0.1228 | 0.0799 | 0.651 | 2.2E-05 | 0.1221 | 0.0806 | 0.66 |
| 12 | -0.242 | -0.024 | 0.1404 | 0.0778 | 0.554 | 2.5E-05 | 0.1382 | 0.0800 | 0.58 |
| 13 | -0.225 | -0.023 | 0.1379 | 0.0648 | 0.470 | 2.9E-05 | 0.1391 | 0.0636 | 0.46 |
| 14 | -0.176 | -0.018 | 0.1134 | 0.0449 | 0.396 | 3.3E-05 | 0.1232 | 0.0351 | 0.28 |
| 15 | -0.101 | -0.010 | 0.0684 | 0.0227 | 0.331 | 3.8E-05 | 0.0915 | -0.0004 | 0.00 |
| 16 | -0.011 | -0.001 | 0.0073 | 0.0022 | 0.302 | 4E-05 | 0.0460 | -0.0365 | -0.79 |
| 17 | 0.080 | 0.040 | -0.0307 | -0.0093 | 0.302 | 4E-05 | 0.0168 | -0.0568 | -3.38 |
| 18 | 0.080 | 0.040 | -0.0300 | -0.0100 | 0.331 | 3.8E-05 | 0.0161 | -0.0561 | -3.48 |
| 19 | 0.080 | 0.040 | -0.0294 | -0.0106 | 0.363 | 3.5E-05 | 0.0154 | -0.0554 | -3.60 |
| 20 | 0.080 | 0.040 | -0.0287 | -0.0113 | 0.396 | 3.3E-05 | 0.0147 | -0.0547 | -3.72 |
| 21 | 0.080 | 0.040 | -0.0279 | -0.0121 | 0.432 | 3.1E-05 | 0.0140 | -0.0540 | -3.85 |
| 22 | 0.080 | 0.040 | -0.0272 | -0.0128 | 0.470 | 2.9E-05 | 0.0134 | -0.0534 | -3.99 |
| 23 | 0.080 | 0.040 | -0.0265 | -0.0135 | 0.511 | 2.7E-05 | 0.0127 | -0.0527 | -4.14 |
| 24 | 0.080 | 0.040 | -0.0257 | -0.0143 | 0.554 | 2.5E-05 | 0.0121 | -0.0521 | -4.31 |

Fig 7.15b indicates that the fluxes do not all cross the zero line at the same time for the Penman-Monteith method. This is indeed more realistic. Also note that at night there is still a positive latent heat flux. This is partially balanced by a greater negative sensible heat flux than in the previous method. Physically, this means that enough heat is lost from the air to the ground to balance both the radiative loss and to also support evaporation from the surface at night. During the day, the sensible heat flux becomes negative well before the radiative forcing becomes zero near sunset.

Finally, Fig 7.15c most graphically demonstrates the differences between the two methods. By looking at the Bowen ratio, we see that the two methods give close to the same answer only during mid-day. At other times, they differ significantly from each other, even having opposite signs at night. It appears that the Penman-Monteith method has the potential for giving better results, assuming that appropriate values can be estimated for the parameters such as relative humidity, ground moisture, etc.

## 7.6 Flux To and From the Ground

We will use the words ***ground flux*** to represent heat flux into the ground measured at the top of the soil. This flux is a small, but not insignificant, component of the surface energy budget. This flux is also related to the surface skin temperature, which is what the atmosphere "sees" when it radiatively looks down at the bottom boundary. If the flux is not known or measured directly, then we often need to parameterize it for PBL forecast models. Sample parameterizations are given below.

### 7.6.1 Simple Parameterizations

Averaged over a full 24-hour cycle, the net heat flux is often near zero. Namely, the heating of the ground during the day is nearly balanced by cooling at night, leading to little net change of heat in the soil. Thus, for some climate and general circulation models (*GCM*), it is assumed for simplicity that $Q_G = 0$.

If we choose to use a flux partitioning scheme such as discussed in Section 7.5, then we could partition some portion of flux to go into or from the ground. One simple scheme is to assume that the ground flux is a percentage, X, of the net radiation:

$$Q_G = X\ Q^* \tag{7.6.1a}$$

where $X = 0.1$ during the daytime, and $X = 0.5$ at night, for example. Fig 7.16 shows data from a number of daytime measurements over land, where most of the ground flux values are between 5% and 15% of the net radiation.

An alternative is to assume the ground flux is a percentage of the turbulent sensible heat flux into the air:

$$Q_G = 0.3\ Q_H \tag{7.6.1b}$$

Both of these simple schemes assume that the sign of the ground flux is always the same as that of the net radiation or sensible heat flux. The latter scheme would fail in an oasis situation.

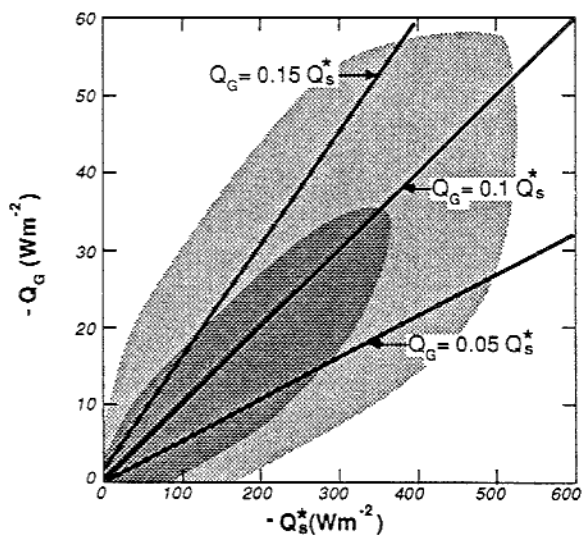


**Fig. 7.16** Range of soil heat flux density $Q_G$ plotted against net radiation for 1040 hourly values during daytime. Darker shadings indicate a higher density of data points. Lines indicate various approximations. (After DeBruin, personal communication).

### 7.6.2 Multilevel Soil Model

At the opposite end of sophistication is a multilevel or analytical model of the soil, where prognostic equations are solved for the temperature at a large number of depths in the soil. Fig 7.17 shows a typical temperature variation over a diurnal cycle in the soil and the atmosphere. Note the scale change for the height-depth axis. Most of the temperature variation in the soil happens within the top 20 centimeters. Below about one meter there is little temperature change associated with the daily cycle, although the annual cycle signal is much larger at that depth.

Since molecular conduction is the primary transport process, we can write the ground flux at any depth as:

$$Q_g = -k_g \frac{\partial T}{\partial z} \qquad (7.6.2a)$$

where $k_g$ is the thermal molecular conductivity of the soil, and $Q_G = Q_g(z=0)$. Appendix C lists examples of the conductivy for a variety of soils.

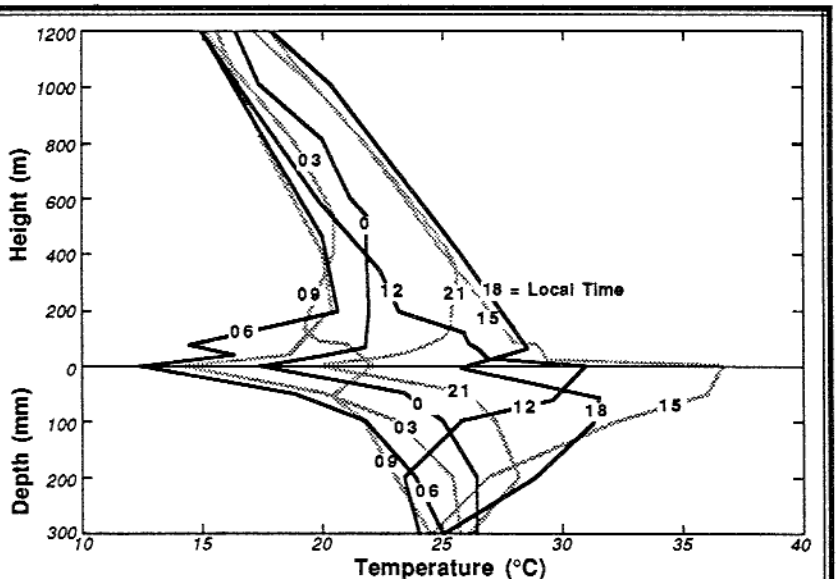


**Fig. 7.17** Three day average of temperature profiles at indicated hours for the Koorin field program, days 7-9. Note the scale difference between height and depth. (After Lettau, personal communication).

Assuming that there are no other sources or sinks of heat in the soil, the second law of thermodynamics yields the simple prognostic equation:

$$\frac{\partial T}{\partial t} = -\left(\frac{1}{C_g}\right)\frac{\partial Q_g}{\partial z} \qquad (7.6.2b)$$

where $C_g$ is the ***soil heat capacity*** (i.e., soil density times specific heat).

Combining this with the previous equation gives the classical ***heat conduction equation***:

$$\frac{\partial T}{\partial t} = \nu_g \frac{\partial^2 T}{\partial z^2} \qquad (7.6.2c)$$

where $\nu_g = k_g/C_g$ is the ***soil thermal diffusivity***. Typical values for $\nu_g$ are $2.7 \times 10^{-7}$ ($m^2/s$) for snow, $2.0 \times 10^{-7}$ to $1 \times 10^{-6}$ for farms, and $1.5 \times 10^{-7}$ for water. A variety of solutions to this classic equation for various boundary conditions are given in applied mathematics, physics, and engineering texts.

For a soil with uniform thermal diffusivity with depth, the boundary conditions often used are: (1) periodic temperature variation at the surface, and (2) no temperature change

at great depths. The solution is a periodic temperature variation that decreases in amplitude with depth, and increases phase lag with depth, as is sketched in Fig 7.18. If the period of the cycle is $\mathbb{P}$, then the amplitude $\Delta T$ of the wave changes with depth as:

$$\Delta T\,(z) \;=\; \Delta T_{surface} \;\cdot\; \exp\left[\, -z \left\{ \frac{\pi}{\nu_g\, \mathbb{P}} \right\}^{1/2} \right] \qquad (7.6.2d)$$

The time lag $\Delta t$ associated with the phase shift across a depth range $\Delta z$ is:

$$\Delta t \;=\; \left(\frac{\Delta z}{2}\right) \left[ \frac{\mathbb{P}}{\pi\, \nu_g} \right]^{1/2} \qquad (7.6.2e)$$

These equations can be applied to an annual ($\mathbb{P}$ = 1 year) or daily cycle ($\mathbb{P}$ = 1 day).

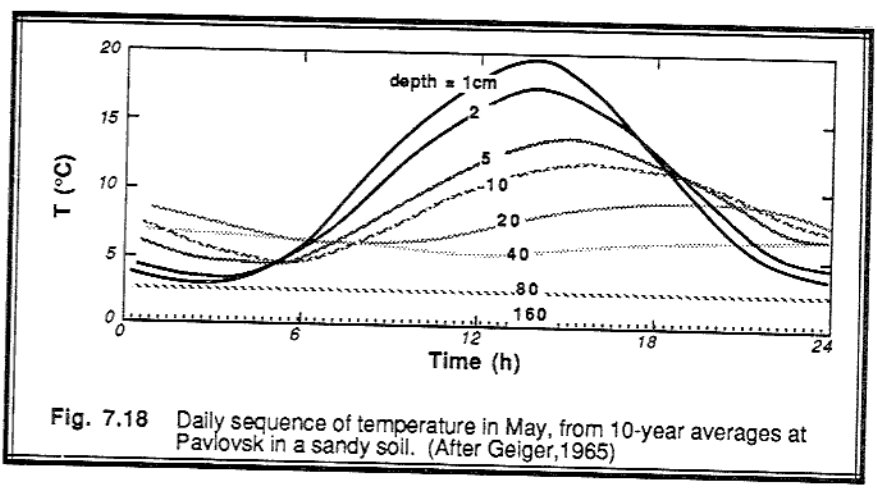


**Fig. 7.18** Daily sequence of temperature in May, from 10-year averages at Pavlovsk in a sandy soil. (After Geiger,1965)

For more realistic nonperiodic forcings or nonuniform soil properties, (7.6.2c) can be solved with a variety of numerical schemes, analytical series expansions or Fourier decompositions. In this way, variations in thermal diffusivity can be included to allow for changes in soil moisture. Since soil moisture depends on precipitation, evaporation, water table level, runoff, and the transpiration of plants, a full detailed parameterization of the soil process often becomes quite complicated.

### 7.6.3 Force-Restore Method

Because most of the soil temperature changes occur within a shallow layer near the surface, Blackadar (1976, 1979; Zhang and Anthes, 1982; Anthes, et al., 1987) suggested a two-layer approximation, where a shallow slab of soil is bounded below by a thick constant-temperature slab (see Fig 7.19).

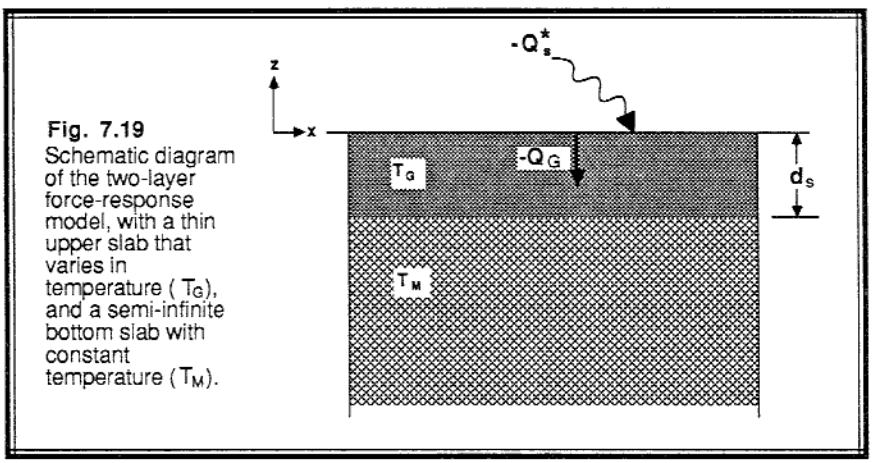


**Fig. 7.19** Schematic diagram of the two-layer force-response model, with a thin upper slab that varies in temperature ( $T_G$), and a semi-infinite bottom slab with constant temperature ($T_M$).

**Concept**. The depth, $d_s$, of the top layer is carefully chosen, based on knowledge of the full solutions from the previous section: $d_s = [(\nu_g \mathbb{P})/(4\pi)]^{1/2}$ . This is the effective depth that "feels" the diurnal cycle, and is on the order of several centimeters for a daily cycle in a desert. We see that longer-period cycles are felt over a deeper depth.

Knowing this critical depth, a soil heat capacity per unit area, $C_{GA}$, can then be found for the surface soil slab: $C_{GA} = C_g \cdot d_s$. Typical values of the heat capacity per unit volume are $C_g = 1\text{x}10^6$ (J m$^{-3}$ K$^{-1}$) for snow, $1.3\text{x}10^6$ for deserts, $3\text{x}10^6$ to $5\text{x}10^6$ for farms, and $1\text{x}10^6$ for muddy water.

With these definitions, the energy balance (7.2b) can be rewritten as a forecast equation for the temperature of the surface slab (Anthes, et al., 1987):

$$C_{GA} \frac{\partial T_G}{\partial t} = -Q_s^* - Q_H - Q_E + Q_G \qquad (7.6.3a)$$

In Blackadar's original formulation, the heat fluxes into the ground and air were parameterized directly, and the latent heat flux was neglected:

$$\frac{\partial T_G}{\partial t} = \frac{-Q_s^*}{C_{GA}} + \left(\frac{2\pi}{\mathbb{P}}\right)\left[T_M - T_G\right] - a_{FR}\left[T_G - \overline{T}_{air}\right] \qquad (7.6.3b)$$

I II III IV

The temperature (term I) of the top slab is assumed to respond to the net radiation forcing (term II), to conduction from the deeper slab (term III) and to turbulent transport with the air (term IV). In other words, the flux from the deep soil tends to ***restore*** the surface

slab temperature, opposing the radiative ***forcing***. The temperature of the bottom slab, $T_M$, is assumed to be a quasi-constant boundary condition. The ground flux can be found from:

$$-Q_G = C_{GA}\left(\frac{\partial T_G}{\partial t}\right) + \left[2\pi \frac{C_{GA}}{\mathbb{P}}\right]\left[T_G - T_M\right] \qquad (7.6.3c)$$

Both of these equations can be solved numerically by stepping forward in time from some known initial condition.

We recognize "$a_{FR}$" as a form of "conductivity" between the ground and the air. Blackadar suggested a magnitude on the order of $a_{FR} = 2\pi/\mathbb{P}$, or $3\text{x}10^{-4}$ s$^{-1}$ for $T_G > T_{air}$ (e.g., daytime), and $1\text{x}10^{-4}$ s$^{-1}$ for $T_G < T_{air}$ (e.g., nighttime).

This two layer force-restore model has become a popular compromise between the more complex multilayer soil model of the previous section, and the overly simplistic approximations of Section 7.6.1. Deardorff (1978) extended this approach to model soil moisture in order to estimate the latent heat flux.

### Example

**Problem**: Make a 24 hour forecast of $Q_H$ , $Q_G$ , $T_G$, and $T_{air}$ for farmland near Wausau, Wisconsin, starting at 12 UTC on 25 April (day 116). Assume a sky covered with 10% low clouds, no middle clouds, and 60% high clouds. Assume that the albedo is 0.2, $T_G$ = 10°C, and $z_i$ = 1000 m and is constant. For initial conditions, start with an air temperature of 8.4°C and a soil surface-slab temperature of 4.5°C. Assume a dry soil (i.e., no latent heat flux).

**Solution**: To make the desired forecast, we must also specify the net radiative flux $-Q^*_s$. We can utilize the parameterization (7.3.2c) for $-Q^*_s$, because we know the latitude and longitude of Wausau (44.97N, 89.63W) and we know the cloud cover.

First, we estimate the soil diffusivity to be $5\text{x}10^{-7}$ m$^2$/s, and $C_g = 1.67\text{x}10^6$ J m$^{-3}$ K$^{-1}$ for farmland, based on the tables in Appendix C. Next, we must calculate the values for $d_s$ and $C_{GA}$ based on the equations of the previous section. We find that the soil slab depth is $d_s$ = 5.9 cm, and the soil heat capacity per unit area (converted to kinematic units) is $C_{GA}$ = 80.33 m, assuming a 24-hour time period for the cyclic forcing.

Table 7-6 shows just the first portion of the resulting forecast of fluxes and temperatures, taking a 15 minute timestep. A longer timestep would have lead to errors for this case.

**Table 7-6.** Example of a ground flux forecast using the force-restore method.

```
Enter the Julian day of the year (Example: April 9, 1984 = 100):    100.000
Enter forecast start time (UTC) in hours:          12.0000
Enter forecast duration in hours:                  24.0000
Enter latitude in degrees (positive North):        44.9700
Enter longitude in degrees (positive West):        89.6300
Enter the low, mid, and high cloudcover fractions:      0.1000     0.0000     0.6000
Enter the albedo:                                   0.2000
Enter Cg, the soil heat capacity/area (m)          80.3300
Enter the deep ground temperature TM (C):          10.0000
Enter the initial surface soil temp TG (C):         4.5000
Enter the initial air temperature (C):              8.4000
Enter the boundary layer thickness (m):          1000.00
```

| T (HR) | -QSTAR(KM/S) | -QG(KM/S) | QH(KM/S) | TG(C) | TAIR(C) |
|---|---|---|---|---|---|
| 12.0000 | -0.0322 | 0.0023 | -0.0345 | 4.8505 | 8.3689 |
| 12.2500 | -0.0127 | 0.0196 | -0.0323 | 5.3625 | 8.3399 |
| 12.5000 | 0.0073 | 0.0359 | -0.0286 | 6.0161 | 8.3142 |
| 12.7500 | 0.0277 | 0.0514 | -0.0237 | 6.7937 | 8.2928 |
| 13.0000 | 0.0483 | 0.0660 | -0.0177 | 7.6793 | 8.2769 |
| 13.2500 | 0.0690 | 0.0798 | -0.0108 | 8.6581 | 8.2671 |
| 13.5000 | 0.0898 | 0.0862 | 0.0036 | 9.6463 | 8.2704 |
| 13.7500 | 0.1104 | 0.0824 | 0.0281 | 10.5353 | 8.2956 |
| 14.0000 | 0.1309 | 0.0814 | 0.0494 | 11.3619 | 8.3401 |
| 14.2500 | 0.1509 | 0.0822 | 0.0687 | 12.1480 | 8.4020 |
| 14.5000 | 0.1705 | 0.0840 | 0.0865 | 12.9064 | 8.4798 |
| 14.7500 | 0.1894 | 0.0863 | 0.1032 | 13.6435 | 8.5726 |
| 15.0000 | 0.2076 | 0.0887 | 0.1190 | 14.3619 | 8.6797 |
| 15.2500 | 0.2249 | 0.0909 | 0.1340 | 15.0617 | 8.8003 |
| 15.5000 | 0.2411 | 0.0929 | 0.1482 | 15.7411 | 8.9336 |
| 15.7500 | 0.2562 | 0.0946 | 0.1616 | 16.3976 | 9.0791 |
| 16.0000 | 0.2700 | 0.0958 | 0.1742 | 17.0279 | 9.2359 |
| 16.2500 | 0.2824 | 0.0965 | 0.1859 | 17.6285 | 9.4032 |
| 16.5000 | 0.2934 | 0.0967 | 0.1967 | 18.1956 | 9.5803 |
| 16.7500 | 0.3028 | 0.0964 | 0.2064 | 18.7256 | 9.7660 |
| 17.0000 | 0.3106 | 0.0955 | 0.2151 | 19.2150 | 9.9596 |
| 17.2500 | 0.3166 | 0.0941 | 0.2226 | 19.6604 | 10.1599 |
| 17.5000 | 0.3210 | 0.0921 | 0.2288 | 20.0588 | 10.3659 |
| 17.7500 | 0.3235 | 0.0897 | 0.2338 | 20.4076 | 10.5763 |
| 18.0000 | 0.3242 | 0.0867 | 0.2375 | 20.7043 | 10.7901 |
| 18.2500 | 0.3231 | 0.0832 | 0.2399 | 20.9471 | 11.0060 |
| 18.5000 | 0.3202 | 0.0793 | 0.2409 | 21.1344 | 11.2228 |
| 18.7500 | 0.3156 | 0.0750 | 0.2406 | 21.2652 | 11.4393 |
| 19.0000 | 0.3092 | 0.0703 | 0.2388 | 21.3387 | 11.6543 |
| 19.2500 | 0.3011 | 0.0653 | 0.2358 | 21.3550 | 11.8665 |
| 19.5000 | 0.2914 | 0.0600 | 0.2314 | 21.3142 | 12.0747 |
| 19.7500 | 0.2801 | 0.0544 | 0.2257 | 21.2172 | 12.2778 |
| 20.0000 | 0.2674 | 0.0486 | 0.2187 | 21.0651 | 12.4747 |
| 20.2500 | 0.2533 | 0.0427 | 0.2106 | 20.8595 | 12.6642 |
| 20.5000 | 0.2380 | 0.0367 | 0.2013 | 20.6025 | 12.8454 |
| 20.7500 | 0.2215 | 0.0306 | 0.1910 | 20.2963 | 13.0173 |
| 21.0000 | 0.2041 | 0.0244 | 0.1797 | 19.9437 | 13.1790 |
| 21.2500 | 0.1858 | 0.0183 | 0.1674 | 19.5477 | 13.3297 |
| 21.5000 | 0.1667 | 0.0123 | 0.1544 | 19.1116 | 13.4686 |
| 21.7500 | 0.1470 | 0.0064 | 0.1406 | 18.6388 | 13.5952 |
| 22.0000 | 0.1269 | 0.0006 | 0.1263 | 18.1331 | 13.7088 |
| 22.2500 | 0.1064 | -0.0050 | 0.1114 | 17.5981 | 13.8091 |
| 22.5000 | 0.0857 | -0.0104 | 0.0961 | 17.0378 | 13.8956 |

**Discussion**: Fig 7.20a &b show plots of the fluxes and temperature. We see that the ground flux changes sign well before sunset. The negative ground flux that follows implies an upward transport of heat from the ground to the surface. When this is added to the incoming radiation $-Q^*_s$, we see that the sensible heat flux $Q_H$ becomes larger than $-Q^*_s$ in the late afternoon.

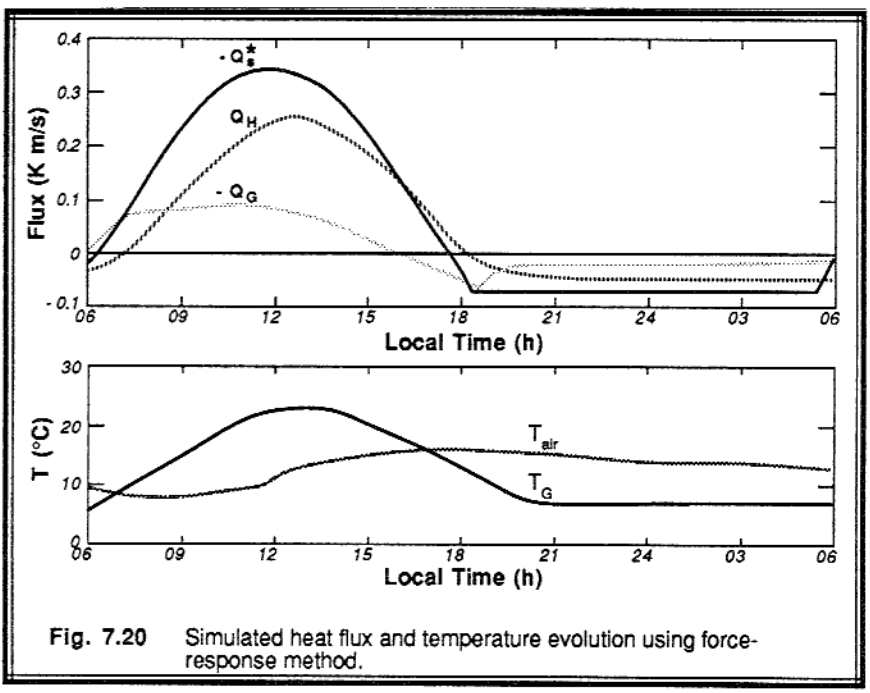


**Fig. 7.20** Simulated heat flux and temperature evolution using force-response method.

The magnitude of the ground flux is larger near sunset than later at night. This is related to the fact that the ground has some thermal inertia, leaving the ground temperature warmer than the air temperature during a few hours near sunset when the ground flux has already become negative. During this short period, the ground is loosing heat not only to the cooler air, but also by radiation to space. This causes the temporary bulge in ground flux at night. Later at night, the ground finally becomes colder than the air, allowing some of the heat lost to space to be replaced by conduction from the air.

## 7.7 References

Anthes, R.A., E.-Y. Hsie, and Y.-H. Kuo, 1987: *Description of the Penn State/NCAR Mesoscale Model Version 4 (MM4)*. NCAR Tech. Note NCAR/TN-282+STR. Boulder, CO. 66pp.

Anthes, R.A. and D. Keyser, 1979: Tests of a fine-mesh model over Europe and the

United States. *Mon. Wea. Rev.*, **107**, 963-984.

Blackadar, A.K., 1976: Modeling the nocturnal boundary layer. *Third Symposium on Atmospheric Turbulence, Diffusion and Air Quality*, Raleigh, NC, Oct 19-22. Amer. Meteor. Soc., 46-49.

Blackadar, A.K., 1979: Modeling pollutant transfer during daytime convection. *Fourth Symposium on Turbulence, Diffusion and Air Pollution*. Reno, NV, Jan 15-18. Amer. Meteor. Soc., 443-447.

Bolton, D., 1980: The computation of equivalent potential temperature. *Mon. Wea. Rev.*, **108**, 1046-1053.

Brutsaert, W.H., 1985: *Evaporation and the Atmosphere*. Reidel. 299pp.

Burridge, D.M., and A.J. Gadd, 1974: The Meteorological Office Operational 10 Level Numerical Weather Prediction Model (December 1974). British Met. Office Tech. Notes Nos. 12 and 48. London Rd., Bracknell, Berkshire, RG12 2SZ, England. 57pp.

Charnock, H., 1955: Wind stress on a water surface. *Quart. J. Roy. Meter. Soc.*, **81**, 639.

Deardorff, J.W., 1968: Dependence of air-sea transfer coefficients on bulk stability. *J. Geophys. Res.*, **73**, 2549-2557.

Deardorff, J.W., 1978: Efficient prediction of ground surface temperature and moisture, with inclusion of a layer of vegetation. *J. Geophys. Res.*, **83**, 1889-1903.

DeBruin, H.A.R., 1983: A model for the Priestley-Taylor parameter a. *J. Clim. & Appl. Meteor.*, **22**, 572-578.

DeBruin, H.A.R. and A.A.M. Holtslag, 1982: A simple parameterization of the surface fluxes of sensible and latent heat during daytime compared with the Penman-Monteith concept. *J. Appl. Meteor.*, **21**, 1610-1621.

DeBruin, H.A.R. and J.Q. Keijamn, 1979: The Priestley-Taylor evaporation model applied to a large shallow lake in the Netherlands. *J. Appl. Meteor.*, **18**, 898-903.

Gadd, A.J., and F.J. Keers, 1970: Surface exchange of sensible and latent heat in a 10-level model atmosphere. *Quart. J. Roy. Meteor. Soc.*, **96**, 297-308.

Garratt, J. R., 1977: Review of drag coefficients over oceans and continents. *Mon. Wea. Rev.*, **105**, 915-929.

Geiger,R., 1965: *The Climate Near the Ground*. Harvard University Press, Cambridge. 611pp.

Grant, A.L.M. and R. Whiteford, 1987: Aircraft estimates of the geostrophic drag coefficient and the Rossby similarity functions A and B over the sea. *Bound.-Layer Meteor.*, **39**, 219-231.

Greenhut, G.K., 1982: Stability dependence of fluxes and bulk transfer coefficients in a tropical boundary layer. *Bound-Layer Meteor.*, **24**, 253-264.

Huband, N.D.S. and J.L. Monteith, 1986: Radiative surface temperature and energy balance of a wheat canopy. Parts 1 and 2. *Bound.-Layer Meteor.*, **36**, 1-17.

Joffre, S.M., 1982: Momentum and heat transfers in the surface layer over a frozen sea. *Bound.-Layer Meteor.*, **24**, 211-229.

Kondo, J. and A. Kawanaka, 1986: Numerical study on the bulk heat transfer coefficient for a variety of vegetation types and densities. *Bound.-Layer Meteor.*, **37**, 285-296.

Kondo, J. and H. Yamazawa, 1986a: Bulk transfer coefficient over a snow surface. *Bound.-Layer Meteor.*, **34**, 123-135.

Kondo, J. and H. Yamazawa, 1986b: Aerodynamic roughness over an inhomogeneous ground surface. *Bound.-Layer Meteor.*, **35**, 331-348.

Kraus, E.B., 1972: *Atmosphere-Ocean Interaction.* Oxford Monographs on Meteorology. Clarendon Press, Oxford. 275pp.

Kyle, H.L., P.E. Ardanuy, and E.J. Hurley, 1985: The status of the Nimbus-7 earth-radiation-budget data set. *Bull. Am. Meteor. Soc.*, **66**, 1378-1388.

Louis, J. F., 1979: A parametric model of vertical eddy fluxes in the atmosphere. *Bound.-Layer Meteor.*, **17**, 187-202.

Mahrt, L. and M. Ek, 1984: The influence of atmospheric stability on potential evaporation. *J. Clim. & Appl. Meteor.*, **23**, 222-234.

McNaughton, K.G., 1976: Evaporation and advection, Parts 1 and 2. *Quart. J. Royal Meteor. Soc.*, **102**, 181-191.

McNaughton, K.G. and P.G. Jarvis, 1983: Predicting effects of vegetation changes on transpiration and evaporation. In T.T. Kozlowski (Ed.), *Water Deficits and Plant Growth.* Academic Press. 1-47.

Monteith, J.L., 1965: Evaporation and environment. *Symp. Soc. Exp. Biol.*, **19**, 205-234.

Oke, T.R., 1978: *Boundary Layer Climates.* Halsted Press, NY. 372pp.

Penman, H.L., 1948: Natural evaporation from open water, bare soil, and grass. *Proc. Roy. Soc. London*, **A193**, 120-195.

Priestly, C.H.B. and R.J. Taylor, 1972: On the assessment of surface heat flux and evaporation using large-scale parameters. *Mon. Wea. Rev.*, **100**, 81-92.

Ripley, E.A. and R.E. Redmann, 1976: Grassland. *In Vegetation and the Atmosphere, Vol. 2, Case Studies.* (Ed. by J.L. Monteith). Academic Press, London. 349-398.

Singh, B. and R. Taillefer, 1986: The effect of synoptic-scale advection on the performance of the Priestley-Taylor evaporation formula. *Bound.-Layer Meteor.*, **36**, 267-282.

Taylor, G.I., 1916: Conditions at the surface of a hot body exposed to the wind, *Brit. Adv. Com. Aero. Rep. and Memor.*, 272.

Verma, S.B., D.D. Baldocchi, D.E. Anderson, D.R. Matt, R.J. Clement, 1986: Eddy fluxes of $CO_2$, water vapor, and sensible heat over a deciduous forest. *Bound.-Layer Meteor.*, **36**, 71-91.

Wallace, J.M. and P.V. Hobbs, 1977: *Atmospheric Science, An Introductory Survey.* Academic Press, NY. 467pp.

Zhang, D. and R.A. Anthes, 1982: A high-resolution model of the planetary boundary layer — sensitivity tests and comparisons with SESAME-79 data. *J. Appl. Meteor.*, **21**, 1594-1609.

## 7.8 Exercises

1) Derive equation (7.3.1c) using basic geometric principles. (Note, there are other equivalent forms of this equation, based on various triginometric identities.)
2) What is the local sun angle above the horizon at 1900 UTC on 25 December at
   a) Madison, Wisconsin
   b) Christmas Island (Line Islands)
   c) Seattle Washington
   d) Tallahassee, Florida
   e) Munich, W.Germany
   f) Barrow, Alaska?
3) Estimate the net radiation, $Q^*$, at Madison, Wisconsin on 25 June at noon local daylight time, if there are 2/8 cirrus clouds and 3/8 cumulus clouds.
4) Based on the discussion of atmospheric conductance in section 7.4, if atmospheric resistance is defined as the inverse of conductance, then what are the units and typical magnitude of atmospheric resistance?
5) Estimate the 10 m drag ($C_D$) and heat transfer ($C_H$) coefficients over land, given $z_o$ = 1 cm, and the Obukhov length = 20 m. How would they differ if the static stability were neutral?
6) Given the following data, estimate the values of
   a. $I^*$
   b. $Q^*$
   c. $Q_H$
   d. $Q_E$
   e. Bowen ratio

   Given: location is Clam Lake, WI (a town with albedo = 20%)
   Latitude = 46 deg 10 min N
   Longitude = 90 deg 54 min W
   Local time of day is 10 AM CST (central standard time = local time = UTC - 6 h)
   Date is April 10, 1981
   Cloud cover is 50% of sky covered by altocumulus
   Surface relative humidity is 80 %
   Anemometer-level humidity is 60 %
   wind is 5 m/s
   Surface temp is 15°C

   Use the methods discussed in the surface forcings section of boundary layer characteristics.
7) Using the desert $Q^*$ data below, apply the force-restore method to calculate the heat flux into the ground and the ground temperature for at least the following times of day: 8, 12, 16, & 24 local time. Justify all assumptions. Assume that the deep soil temperature is 20°C.

| Local time: | 4 | 6 | 8 | 10 | 12 | 14 | 16 | 18 | 20 | 22 | 24 | 02 |
|---|---|---|---|---|---|---|---|---|---|---|---|---|
| $Q^*$ ($J\ m^{-2}s^{-1}$): | -80 | -20 | 100 | 300 | 500 | 600 | 400 | 50 | -120 | -110 | -100 | -90 |

8) Based on the following instantaneous measurements of potential temperature ($\theta$), specific humidity (q), and vertical velocity (w), find the Bowen ratio.

| $\theta$ (°C) | q (g/kg) | w (m/s) |
|---|---|---|
| 22 | 10 | 0.1 |
| 21 | 12 | 0.5 |
| 18 | 12 | -0.4 |
| 20 | 6 | -0.2 |
| 19 | 10 | 0 |

9) State some reasons why one might need to use geostrophic drag relationships.

10) [Problems 10 and 11 are identical to the solved examples in the text. We recommend that the instructor modify the problem to any other location and time of interest to the students.] What is the value of the net radiation ($Q^*$) absorbed at the earth's surface as a function of time (for a 24 hour period) under the following conditions:

albedo = 0.2
location = farmland near Wausau, Wisconsin
date = April 9, 1982
cloudcover: low= 10% mid = 0 high = 60%

Plot your result (start the graph at 6 AM).

11) Given the following conditions:

same situation as problem (10).
deep soil temperature is 10°C.
soil is dry ($Q_E = 0$).
BL remains 1 km thick.
potential temperature is constant with height (but not time).
no advection or entrainment into the BL.
Initial conditions (at 6 AM): $T_{air} = 8.4°C$, and $T_G = 4.5°C$

Calculate and plot the following as a function of time for a 24 hour period starting at 6 AM. Use the force-restore method for the ground temperature, and turbulence equations for mean flow for the air temperature.

a) $T_{air}$
b) $T_G$
c) $Q_G$
d) $Q_H$

12) SITUATION: Daytime boundary layer over land (N. America).
OBSERVATIONS:

| Height , z (m) | 12 | 8 | 2 | $0.1=z_o$ | (m) |
|---|---|---|---|---|---|
| $\theta$ | 300 | 301 | 303 | 308 | (K) |
| U | 5.4 | 5.0 | 3.4 | 0 | (m/s) |

What are the values of: a) $C_{DN}$ b) $C_D$

13) For sandy clay with 15% moisture, at what depth below the surface will the diurnal temperature variations be 1 % of the surface temperature variations?

14) Given a 1km constant thickness boundary layer with initial $\theta$ = 10°C flowing at M=10 m/s over land, where the land has the same surface temperature as that of the air near the surface. At some point, the air leaves the land and flows over the ocean, where the ocean sea surface temperature is 20°C and the pressure is 100 kPa. Assume that the boundary layer is well mixed. Calculate and plot the heat flux $Q_H$ and the boundary layer temperature as a function of distance from the shoreline.

15) For a pressure gradient of 0.2 kPa / 100 km and a surface roughness length of $z_o$ = 2 cm, find:
a) the value of the surface Rossby number
b) the value of the neutral geostrophic drag coefficient
c) $u_*$ , assuming statically neutral conditions

16) Given a drag coefficient of $3 \times 10^{-3}$ at $R_i$ = -0.4 and $z_s$ = 10 m, how would the drag coefficient change if z = 100 m?

17) What is the roughness length, $z_o$, over the ocean for a wind speed of 40 m/s ?

18) What is the time lag of the diurnal cycle of temperature at a depth of 15 cm in farmland? What will be the amplitude of the temperature wave at that depth?

19) Use equation (7.5.2b) to calculate and plot $s_{cc}(T)$ vs T, and compare your answer with Fig 7.13.

20) For a temperature of 20°C, dew point of 10°C, ground surface relative humidity of $X_o$ = 80%, and wind speed of 5 m/s, find $Q_H$ and $Q_E$ using:
a) Priestley-Taylor method
b) Penman-Monteith method
(Hint: use the result from the previous question.)

21) Verify that the surface energy balance equation is satisfied using the $Q_H$ and $Q_E$ parameterizations from:
a) The Bowen ratio method (equations 7.5.1 b & c)
b) The Priestley-Taylor Method (equations 7.5.2e & f)
c) The Penman-Monteith method (equations 7.5.3a & b).